
A thermomechanical analysis of the central column tiles

René Chavan, CRPP / EPFL - Lausanne, 1998 - 1999.

Internal report INT 195/99.

Abstract. *The analytical and computational techniques to assess the thermomechanical sollicitation of graphite tiles of the central column are presented. Three-dimensional, non-linear and transient temperature and stress-strain calculations performed with a commercially available code (limited problem size in its academic release) are discussed and validated by comparing the numerical results with the values obtained from analytical solutions in a semi-infinite solid with equivalent averaged material properties. The importance of appropriate settings of parameters in the finite element solving steps is emphasized. Aspects of sharing model data and boundary conditions between different computer codes are explained.*

The choice of selecting graphite as a first-wall material in TCV is primarily based on its exceptional physical properties and commercial availability at a reasonable price, as well as easy machinability. Graphite is compatible with ultrahigh vacuum, has a low atomic number ($z = 12$) and an operation limit in plasma conditions of around 2400 K. The thermophysical properties of graphite explain its high resistance against thermal shock and thermal fatigue. The design of the presently installed second generation first wall tiles (in particular on the central column) has been optimized in terms of power deposition, machineability (cost), thermal stress and strain, and assembly, although the definite finite element code has not been completed before ordering the tiles.

This report puts the case for and sums up a structured approach to solving a real world engineering task, rather than detailing all the theoretical aspects of the various subjects treated. The author would be grateful to anyone who, finding an error or having a comment, communicates this to him. Some illustrations were inserted for completeness in July 2000.

Table of content

1	The mapping of plasma power deposition profiles to thermal surface loads	
2	Physical and derived data for graphite	
3	Analytical solutions for heat conduction and thermal stress in an idealized solid	
3.1	Temperature distribution	11
3.1.1	Solid bounded by two parallel planes	11
3.1.2	Semi-infinite solid	12
3.2	Thermal energy balance	12
3.2.1	Energy contained in a tile.	12
3.2.2	Radiation losses	13
3.2.3	Conduction losses.	14
3.3	Thermal stress and strain	14
3.4	Optimizing the tile thickness versus permissible heat load	15
3.4.1	Heat flow limited by temperature	15
3.4.2	Heat flow limited by thermal stress	16
4	Finite element analysis	
4.1	Summary on mechanical design and installation of the central column tiles in TCV	17
4.2	Geometric description and parametric modeling of the tile cross section	18
4.3	Modelling of linear and non linear material properties	21
4.4	Single and multiple discharge temperature solutions.	22
4.4.1	Heat influx loads and energy balance	22
4.4.2	Radiative and conductive boundary conditions	23
4.4.3	Solver options and parameters	24
4.5	Thermomechanical stress solution	25
4.5.1	Failure criteria	25
4.5.2	Initial temperature boundary conditions and displacement constraints.	27
4.5.3	Solver options and parameters	28
5	Results and conclusions	
5.1	Case list	29
5.2	Discussion	29
6	Code file listing	
7	References	

1 The mapping of plasma power deposition profiles to thermal surface loads

Energy extracted from the plasma core by conduction and convection is either transformed into radiation in a radiating boundary layer or coupled to limiters by particle bombardment. The plasma power deposition in terms of thermal surface load is due to the latter.

The toroidal and poloidal field coils of the tokamak generate a magnetic vector field \mathbf{B} which has components relative to the 'global' coordinate system in the radial r , toroidal ϕ and poloidal z directions at any location C . Due to the rotational symmetry along the (vertical) z axis and the magnetic properties of the divertor target zone, the field components in the vicinity of the central column tile surface are reduced to constant values of $\mathbf{B}_{(x,y,z)} = (B_{r(x,y)}, B_{\phi(x,y)}, B_{z(x,y)})$ evaluated at radius R_I . The radial (along r) and toroidal (tangent to r) components are considered constant in the circular segment delimited between a locus on the tile at radius r and the circumscribed central column radius R_I (R_2 is the inscribed outer wall radius), that is $|B_{r(x,y)}| = cte$, $|B_{\phi(x,y)}| = cte$ and $|B_{z(x,y)}| = cte$.

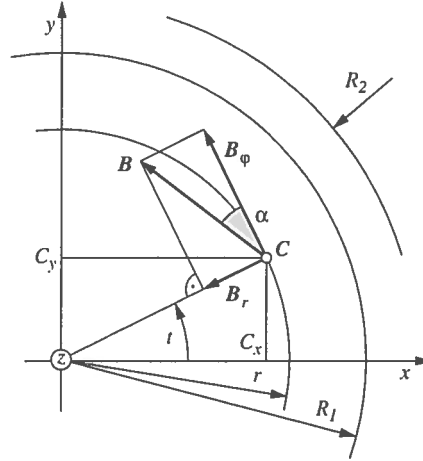


Figure 1.1
Geometry of the magnetic field at $z = \text{constant}$.

Depending on the needs, either cartesian or polar coordinates are used, so for an arbitrary point on the tile surface, we have

$$\mathbf{C}_{(x,y,z)} = r \cdot \begin{bmatrix} \cos t \\ \sin t \\ z/r \end{bmatrix} \quad \text{with} \quad \begin{cases} r^2 = x^2 + y^2 \\ \tan t = y/x \\ r \leq R_I \end{cases} \quad (\text{Equ. 1.1})$$

As shown in figure 1.1, α is the field impact angle along the central column through any point lying on a circle of constant radius R_I . The radial and toroidal magnetic flux density components having constant values depending on the poloidal coordinate z only, α is constant for any given z and can be calculated from the expression

$$\alpha = \arccos \frac{B_{\phi}}{\sqrt{B_r^2 + B_{\phi}^2}} \quad (\text{Equ. 1.2})$$

Assuming only planar relationships of the vector components and in order to simplify the subsequent notation, the z component of all vectors will be omitted where possible. The magnetic field at point C is

$$\mathbf{B}_{(x,y,z)} = \begin{bmatrix} -B_r \cdot \cos t - B_{\phi} \cdot \sin t \\ -B_r \cdot \sin t + B_{\phi} \cdot \cos t \\ \frac{B_z}{B_{\phi}} \cdot t \end{bmatrix} \quad (\text{Equ. 1.3})$$

Ionized particles from the plasma boundary travel on trajectories colinear along magnetic field lines. A field line is defined as a curve in space $\mathbf{r}_{(t)}$, being in a vector field \mathbf{B} , for which

$$\mathbf{B}_{(r)} \times \frac{d\mathbf{r}}{dt} = 0 = \det \begin{bmatrix} B_x & \frac{dr_x}{dt} \\ B_y & \frac{dr_y}{dt} \end{bmatrix} = B_x \frac{dr_y}{dt} - B_y \frac{dr_x}{dt} \quad (\text{Equ. 1.4})$$

meaning in words that the tangent vectors to the field line are always colinear to the magnetic field vectors in any point on the field line. In the present case, the only possible field line vector \mathbf{l} fulfilling (equ. 1.2) and (equ. 1.3) appears to be a *logarithmic spiral* [ref. 18 : A70] as shown in figure 1.2, with the general equation

$$\mathbf{l} = \begin{bmatrix} u \cdot e^{-mt} \\ t \end{bmatrix} \quad (\text{Equ. 1.5})$$

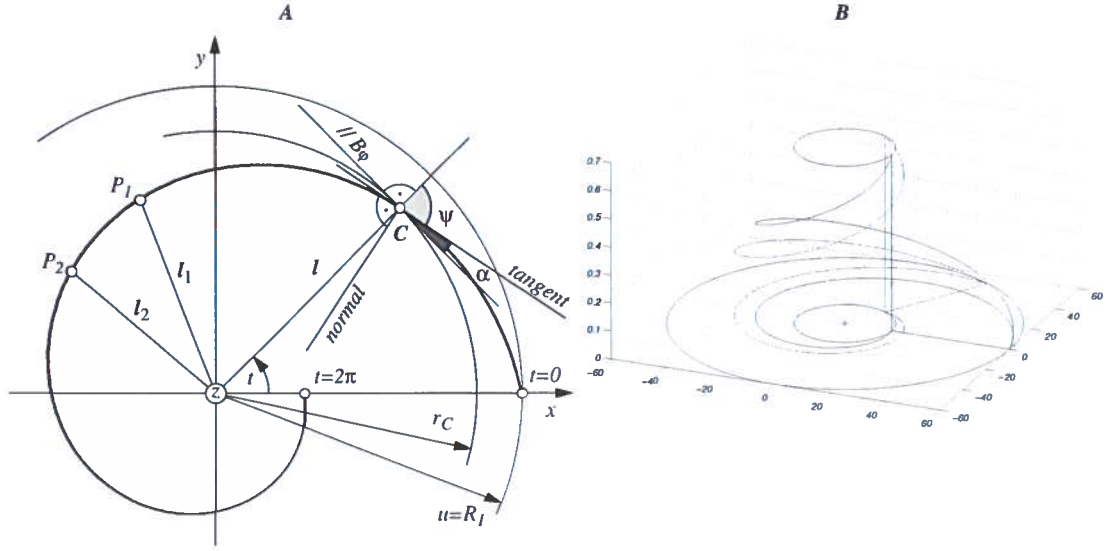


Figure 1.2

Basic geometric definition of a logarithmic spiral (A) and three-dimensional helical fieldlines (B)

The scalar u is considered to be the starting point of the logarithmic *reference spiral*, at $t = t_l = 0$ on the x axis. The index l shall refer to the *reference spiral*, for which we define on the purpose of field line mapping the angle $t = t_l = [0, 2\pi]$, increasing counterclockwise, while the radial component of l decreases exponentially with t_l . The characteristic constant m of all spirals (field lines with constant B_r and B_ϕ at a given z), is expressed in terms of the constant field impact angle α and the constant angle ψ , spanning between the spiral vector l and the corresponding tangent vector t , by the equations

$$\left. \begin{aligned} \psi &= \frac{\pi}{2} - \alpha \\ \tan \psi &= \frac{1}{m} \end{aligned} \right\} \quad m = \frac{1}{\tan\left(\frac{\pi}{2} - \alpha\right)} \quad (\text{Equ. 1.6})$$

As it becomes evident later, the radius of curvature ρ of the spiral will be needed to verify results. This value is obtained in any point of the spiral with

$$\rho = l \cdot \sqrt{1 + m^2} \quad (\text{Equ. 1.7})$$

Per definition the center of ρ lies on the normal to the spiral tangent at any point and therefore does not lie on the spiral radius vector l . It is interesting to remark that the spiral l becomes a simple circle as α , and thus m , tend to zero. From (equ. 1.7) we would get $\rho = l$ - the radius of curvature of the circle. Based on the initial assumptions, no such circular field line can coexist with helical field lines, and therefore $\alpha > 0$ and $\psi < \pi/2$ is always true.

One might be interested in calculating the arc length between two points on the spiral with

$$\overline{P_1 P_2} = \frac{u \cdot \sqrt{1 + m^2}}{m} \cdot e^{-mt} \Big|_{t_1}^{t_2} = \frac{\sqrt{1 + m^2}}{m} \cdot (t_2 - t_1) \quad (\text{Equ. 1.8})$$

For any point lying on the single field line along the reference spiral, (equ. 1.5) gives the appropriate field components. Hence, conveniently in polar coordinates, through any point given by

$$C_{(r,t)} = (r_C, t_C) \quad (\text{Equ. 1.9})$$

and not necessarily on the reference spiral, goes a field line defined by

$$l_C = \begin{bmatrix} u \cdot e^{-mt_l} \\ \tau_C + t_l \end{bmatrix} \quad (\text{Equ. 1.10})$$

where τ_C is the angular value by which the reference spiral l has to be rotated in order to include point C . There is one distinct τ for each point on the tile contour. Different points may have similar values for τ . A negative τ indicates a clockwise rotation of the *reference spiral*.

The rotation of a point C on the tile describes a circular path of radius r_C , centered at the magnetic field origin. Hence τ_C is the angular difference between t_C and the intersection of this circle with the reference spiral at angle t_{Cl} as shown in figure 1.3A. Solving the radial term of (equ. 1.10) for t we get

$$t_{Cl} = \frac{1}{m} \cdot \ln \frac{r_C}{u} \quad (\text{Equ. 1.11})$$

and substituting (equ. 1.11) into the angular term of (equ. 1.10) and solving for τ gives

$$\tau_C = t_C - t_{Cl} \quad (\text{Equ. 1.12})$$

Let us take a closer look at the area limited geometrically by one helical field line on each side, having the same constant m but different values for τ , a circular segment of radius R_I (see figure 1.1 for definition) as the outer edge and a straight line as the inner boundary. The line segments intersection points are defined with A, B, C and D as shown in figure 1.3A. We start with the straight segment \overline{CD} , which may represent a small, randomly chosen arc length of the elliptic tile contour (tile is on the dashed side) approximated with a discrete contour of straight lines. This artifice is necessary as there is no analytical expression to calculate the length of an elliptic segment (see [chap. 4.2] for a parametric description of the tile contour). If necessary and just to mention it, exact arc lengths can be computed for the cylindrical tile segments for higher numerical accuracy. We define the contour such as $D-C$ turns counterclockwise around the tile.

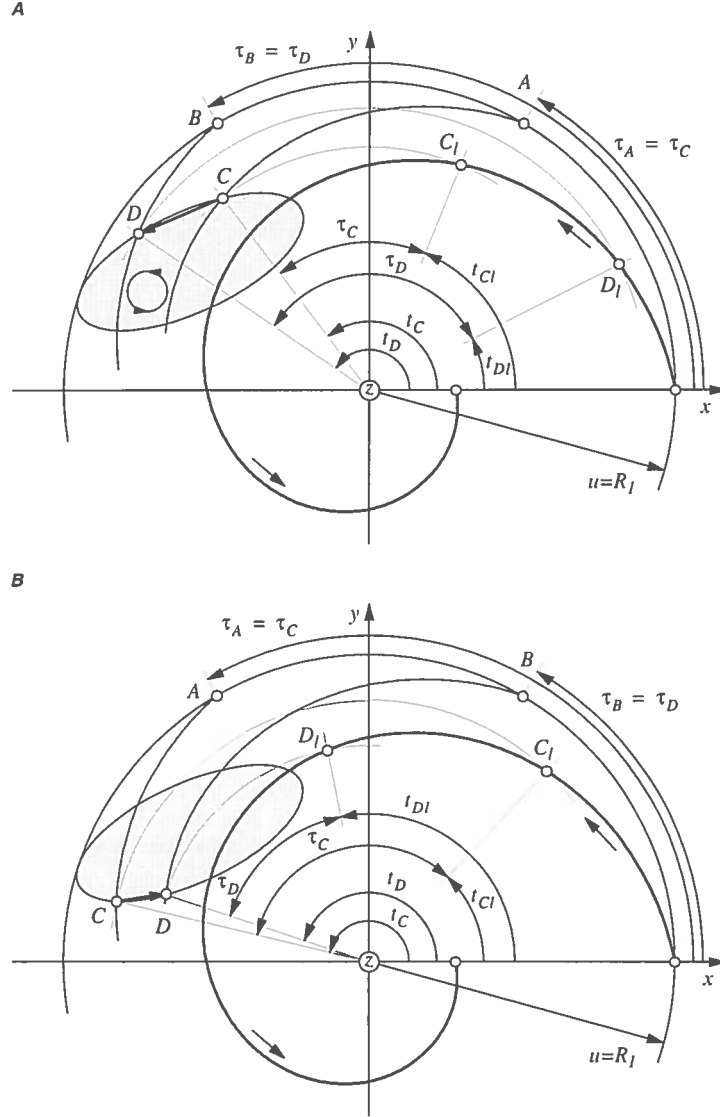


Figure 1.3

How logarithmic spirals represent magnetic field lines : (A) Where the tile receives heat : $\tau_B - \tau_A > 0$; (B) The 'shadowed' part of the tile : $\tau_B - \tau_A < 0$.

In order to determine the heat flux hitting the segment \overline{CD} , one has to establish the power balance over the area $ABCD$. From plasma equilibrium calculations, we know the perpendicular and circumferentially constant heat influx across the circular boundary R_I . As the energy flow from the plasma is coupled to the graphite plates essentially by ionized particle bombardment, heat flow is possible only parallel to field lines. It is therefore legitimate to state that the heat inflow over the arc \overline{AB} is identical to the heat outflow over the segment \overline{CD} . By mapping along their unique field lines the points C to A and D to B , the surface (or arc length in 2D) ratio necessary to calculate the power balance is established.

We have (equ. 1.10) describing the spiral through C - the reference spiral rotated by τ_C . Since C and A lie on the same field line $t_C = t_A$. Because A lies on the circle of radius R_I , the radius at which all spirals (reference and rotated) start with $t_I = 0$ is equal to u . Hence A has the polar coordinates

$$\begin{aligned}
u &= R_1 \\
\tau_A &= \tau_C \\
A_{(r,t)} &= (u, \tau_A) = (u, \tau_C)
\end{aligned} \tag{Equ. 1.13}$$

Repeating the mapping steps (equ. 1.9) to (equ. 1.13) for D on B , in the order appropriate for coding, we obtain

$$\begin{aligned}
D_{(r,t)} &= (r_D, t_D) \\
u &= R_1 \\
t_{DI} &= \frac{1}{m} \cdot \ln \frac{r_D}{u} \\
\tau_D &= t_D - t_{DI} \\
\tau_B &= \tau_D \\
I_D &= \begin{bmatrix} u \cdot e^{-mt_I} \\ \tau_D + t_I \end{bmatrix} \\
B_{(r,t)} &= (u, \tau_B) = (u, \tau_D)
\end{aligned} \tag{Equ. 1.14}$$

With the right indexing (equ. 1.14) are applicable for any point belonging to the tile contour and its image point on the circular boundary R_1 .

The heat flow crossing the boundary line \overline{AB} per unit length of the poloidal coordinate z (in W/m) has to hit the tile on the boundary segment \overline{CD} , leading to

$$p_{\overline{AB}} \cdot \overline{AB} = p_{\overline{CD}} \cdot \overline{CD}$$

Only ratios of scalars are used, so plus or minus signs are not needed in the balance. The tile always receives thermal energy from the plasma. As we found earlier, segment \overline{AB} is a circular arc of the length $u \cdot (\tau_B - \tau_A)$ and \overline{CD} is the length of the vector $|D - C|$, hence (in W/m^2)

$$p_{\overline{CD}} = p_{\overline{AB}} \cdot \frac{u \cdot (\tau_B - \tau_A)}{|D - C|} \tag{Equ. 1.15}$$

A tile surface element is only exposed to a heat flow when it *sees* the field lines. The smaller the length $|D - C|$ the smaller is the value of $(\tau_B - \tau_A)$. In other words the heat flow according to (equ. 1.15) tends towards zero when C and D lie on the same spiral at a very small distance (infinitesimally small). This is the point where the tangent to the tile contour is colinear to the field line :

$$\frac{dr}{dt} \times \frac{dl}{dt} = 0 \tag{Equ. 1.16}$$

So far the relative location of C and D resulted in

$$\tau_B - \tau_A > 0 \quad \text{or in equivalent vector product terms} \quad \frac{dr}{dt} \times \frac{dl}{dt} > 0 \tag{Equ. 1.17}$$

Let us now consider the case

$$\tau_B - \tau_A < 0 \quad \text{or} \quad \frac{dr}{dt} \times \frac{dl}{dt} < 0 \tag{Equ. 1.18}$$

shown in figure 1.3B, where the field lines through C and D intersect with the tile contour twice. \overline{CD} does not see the plasma and lies on the self shadowed side of the tile.

When computing the values for τ along the tile contour, it is *in most cases* sufficient to determine at which point $\tau_B - \tau_A < 0$ occurs and to consider that all remaining points are shadowed. Nevertheless one has to be *very carefull* in cases where the tile contour includes

- some geometric discontinuity, like an edge or a hole;
- a *roof top* like geometry with flat adjacent faces (infinite radius of curvature);
- a concave section, where the curvature is negative.

Depending on the field angle and the geometry of the polygon contour, the 'roof top' tiles of the first generation for example could have a shadowed zone between two irradiated regions. Such a tile contour can be easily identified by calculating the radius of curvature at all tile contour points and comparing it with the radius of curvature of the field line through that same point. This scenario may occur if the radius of curvature of the field line (equ. 1.7) is smaller than the radius of curvature of the tile. In order to be certain about this issue it is recommendable to calculate the difference of τ for all point pairs and to check wheather there is *more than one change of sign*. All points with values smaller than zero receive no heat flow as shown in figure 1.3B.

By now, the *shadowing of the neighbour tile* (on the left or counterclockwise side) can be determined by simply comparing the respective values of τ . From (equ. 1.17) and (equ. 1.18), we know that $\tau_B > \tau_A$ where heat flow hits the tile and $\tau_B < \tau_A$ for shadowed areas of the tile and we can state :

- the *last* point (counterclockwise) intercepting a field line on a given complete tile contour is the one for which τ reaches its *maximum value*.

This means that *no* point of the neighbouring tile having a τ smaller than the largest τ of the preceeding tile can receive power.

The rotational symmetry/periodicity of the central column tiles implies that the first τ calculated for the left side neighbour tile is necessarily equal to the first τ of the main tile minus $\theta/2$ (see [chap. 4.2] for definition of θ).

All fieldlines between these τ_{min} and τ_{max} are mapped on their image arc on the circle of radius R_I . As a result there is no field gap between tiles and there are no missing field lines for which power is not accounted for. If the toroidal spacing between tiles was too large, such as to let field lines hit the steel wall, the wall contour would have to be included in the calculation. The accuracy of the discretized model is computed as the ratio of the total heat received by the tile to the theoretical heat load divided by the number of exposed tiles (32 in this case).

Based on the mapping model presented in this chapter, the power deposition profiles on a 'model' tile have been computed (table 6.1). Even with a rather coarse discretisation of the exposed tile contour ($2 \times 10 + 8$ straight segments), the average cumulated energy loss is $\sim 5\%$. For a normalized power influx into control volume at boundary R_I of 1 MW/m^2 , the power peaks to 4 times this value at the edge of the elliptical area shadowed by the neighboring tile, located at $t = 1.1$ degrees. The tile gap is centered on the x-axis.

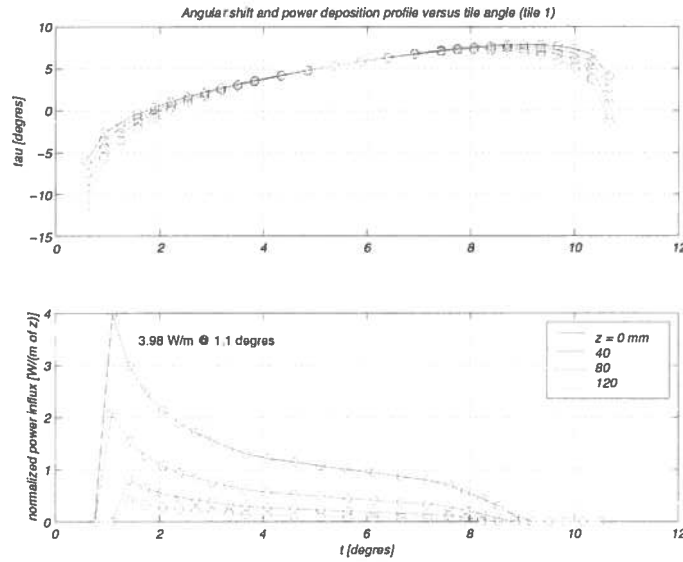


Figure 1.4

Angular power deposition profile on a 'model' tile at 4 different z values.

2 Physical and derived data for graphite

The present material data base is valid for the high purity graphite grade chosen for the central column tiles. It is based on correspondance with the supplier¹, on material test certificates for graphite actually delivered² and on catalogue data³. The graphite is isostatically pressed and the relevant properties are considered isotropic. The open porosity is less than 10 % at an average grain size of 1 - 2 μm . All surfaces are smoothly machined and crack free under visual inspection.

The most helpful parameter for transient temperature calculations is the thermal diffusivity [ref. 4], a measure for how fast the heat energy diffuses through the solid and for the time needed to reach thermal equilibrium within the solid :

$$a = \frac{\lambda}{\rho \cdot c_p} \quad (\text{Equ. 2.1})$$

The behaviour of graphite is highly non linear : the thermal capacity increases by a factor of 2.5 up to 1000 K and changes little above this value. At room temperature graphite has a high thermal conductivity decreasing exponentially at higher temperature. As a result, the thermal diffusivity of graphite decreases by more than an order of magnitude over the relevant temperature range.

Temperature distributions calculated analytically with the assumption of constant coefficients (see [chap. 3.1]) are accurate to about 20 % if average (rather than room temperature) values of thermal conductivity and heat capacity are used [ref. 14]. Thermal stress calculations (see [chap. 3.3]) are based on the averaged value of thermal expansion. In general terms, the average of a temperature variant function $f_{(T)}$, over the temperature interval occuring T_0 to T_1 , is defined by

$$\bar{f} = \frac{1}{T_1 - T_0} \int_{T_0}^{T_1} f_{(T)} dT \quad (\text{Equ. 2.2})$$

As such, the temperature variant data is available at discrete values only, but it is easily fitted with a negligible error margin over a absolute temperature range of 200 to 2400 K to a polynomial function $f_{(T)}$ and it's integral, of degree n in T , with $n+1$ coefficients (as listed below) :

$$f_{(T)} = p_1 T^n + p_2 T^{n-1} + \dots + p_n T + p_{n+1} \quad (\text{Equ. 2.3})$$

$$\int_{T_0}^{T_1} f_{(T)} dT = \left[\frac{1}{n+1} p_1 T^{n+1} + \frac{1}{n} p_2 T^n + \dots + \frac{1}{2} p_n T^2 + p_{n+1} T \right]_{T_0}^{T_1} \quad (\text{Equ. 2.4})$$

$$\lambda_{(T)} = a \cdot T^5 + b \cdot T^4 + c \cdot T^3 + d \cdot T^2 + e \cdot T + f \quad \begin{cases} a = -6.6547 \cdot 10^{-15} & d = 2.7141 \cdot 10^{-4} \\ b = 5.3703 \cdot 10^{-11} & e = -0.2334 \\ c = -1.7027 \cdot 10^{-7} & f = 130.5754 \end{cases} \quad (\text{Equ. 2.5})$$

$$c_{p(T)} = a \cdot T^5 + b \cdot T^4 + c \cdot T^3 + d \cdot T^2 + e \cdot T + f \quad \begin{cases} a = 1.5040 \cdot 10^{-13} & d = -7.8550 \cdot 10^{-3} \\ b = -1.2954 \cdot 10^{-9} & e = 7.3437 \\ c = 4.4675 \cdot 10^{-6} & f = -1.0110 \cdot 10^3 \end{cases} \quad (\text{Equ. 2.6})$$

$$\alpha_{(T)} = a \cdot T^6 + b \cdot T^5 + c \cdot T^4 + d \cdot T^3 + e \cdot T^2 + f \cdot T + g \quad \begin{cases} a = 1.6064 \cdot 10^{-25} & e = 4.7105 \cdot 10^{-12} \\ b = -1.4216 \cdot 10^{-21} & f = 1.1147 \cdot 10^{-9} \\ c = 4.8023 \cdot 10^{-18} & g = 2.3044 \cdot 10^{-6} \\ d = -7.5044 \cdot 10^{-15} \end{cases} \quad (\text{Equ. 2.7})$$

$$\sigma_{t(T)} = a \cdot T^3 + b \cdot T^2 + c \cdot T + d \quad \begin{cases} a = -0.0094 & c = -6.3834 \cdot 10^4 \\ b = 52.7284 & d = 4.7349 \cdot 10^7 \end{cases} \quad (\text{Equ. 2.8})$$

$$\sigma_{f(T)} = a \cdot T^3 + b \cdot T^2 + c \cdot T + d \quad \begin{cases} a = 0.0025 & c = 8.3093 \cdot 10^3 \\ b = -2.2800 & d = 6.2737 \cdot 10^7 \end{cases} \quad (\text{Equ. 2.9})$$

1. SGL Carbon Group, Werk Ringsdorf, D-53170 Bonn.

2. Abnahmeprüfzeugnisse für Reinstgraphit SGL R6650.

3. Graphite Catalogue SGL, 1552e/96.

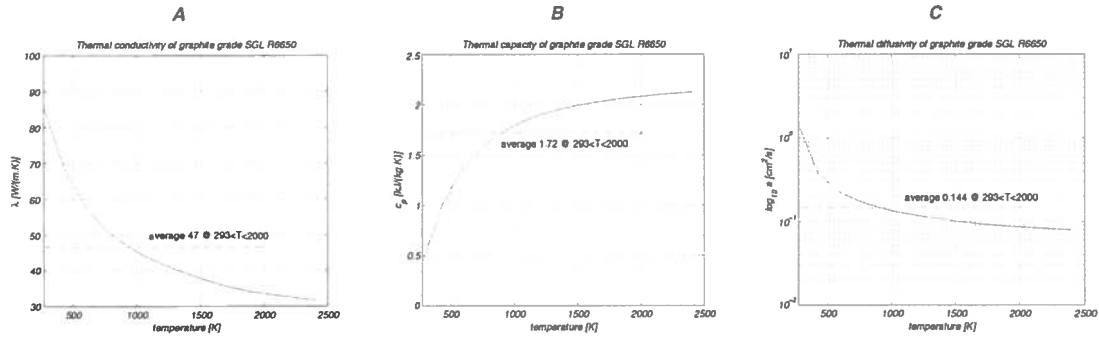


Figure 2.1

Thermal conductivity, capacity and calculated diffusivity of graphite.

The effective emissivity increases above 1400 K. In comparison with rough and oxydized surfaces, the emissivity may decrease by 0.1 if the surface is polished or grinded. Although temperature dependant radiation may be included in the calculation, standard results are based on a constant value of 0.75. Further data is given in [ref. 17 : Ka4].

For reasons discussed in detail in [ref. 1], the mechanical resistance increases with temperature. Mechanical failure mechanisms of graphite are best described by the models applying to brittle ceramic materials [ref. 19]. Although a Weibull distribution for failure probability over a given volume of material is not obtainable within the scope of this project, graphite has a rather low value of fracture toughness [ref. 2] of

$$K_{Ic\infty} = \sigma_c \cdot \sqrt{\pi a_c} = 0.6 - 1.6 \quad \text{MPa}\sqrt{\text{m}} \quad (\text{Equ. 2.10})$$

Given the critical flexure strength the resulting critical crack length is typically

$$a_c = \left(\frac{K_{Ic\infty}}{\sigma_c} \right)^2 \cdot \pi = 0.25 \quad \text{mm} \quad (\text{Equ. 2.11})$$

This value can be interpreted as the theoretical upper limit characteristic size of any internal or surface defect tolerated in and on the tile. Machined geometric features should have a radius of curvature larger than 0.25 mm.

At higher elongation, the stress-strain relationship of graphite deviates noticeably from linear elastic behaviour. In order to obtain the highest possible stresses, a constant upper limit value is assumed for the Young's modulus. Stress induced creep may appear at temperatures above 2300 K.

Partially due to low linear thermal expansion, increasing by a factor of 2 within the temperature range of interest, graphite offers a remarkable thermal shock resistance [ref. 3, based on a two dimensional stress state] calculated as :

$$R_s = \frac{\sigma_c(1-\nu)}{\alpha E} > 940 \text{ } ^\circ\text{C} \quad (\text{Equ. 2.12})$$

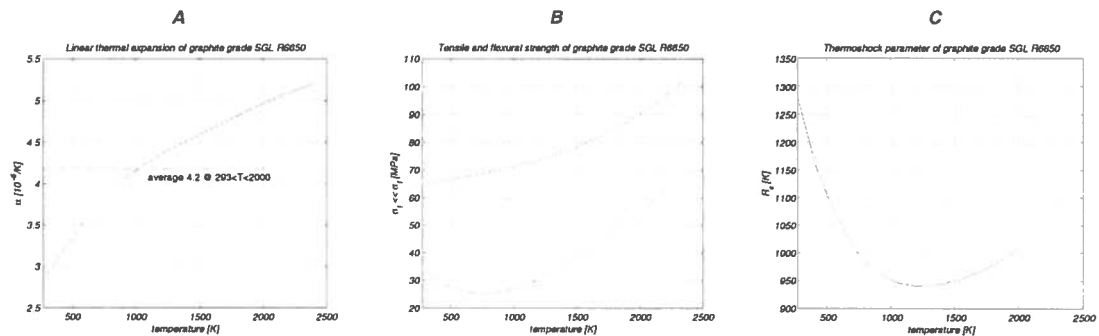


Figure 2.2

Thermal expansion, strength and thermoshock resistance of graphite.

Both fracture toughness and thermal shock resistance rely on the adequate experimental determination of the elastic modulus $E = \sigma/\epsilon \cong 13.5 \cdot 10^9 \text{ Pa}$ and the shear modulus $G = \tau/\phi \cong 5.4 \cdot 10^9 \text{ Pa}$. As mentioned earlier in this chapter, we consider graphite to be 'reasonably' isotropic. In practice, this might not be the case as graphite powder processing techniques, though isotatic, do not guarantee perfect isotropy. The various production lots do have different characteristics¹. Results should be interpreted with these restrictions in mind. Complementary information is found in [ref. 19 : chapter 2.5].

1. Abnahmeprüfzeugnisse für Reinstgraphit SGL R6650.

Poisson's ratio $\nu = 0.25$ is generally obtained from the relationship $E = 2G(1 + \nu)$.

Beside the isothermal compressive strength value of 150 MPa, the graphite manufacturer provides both tensile and flexure strength test data measured at different temperatures. Based on results outlined later in [chap. 5] reveal, it is appropriate to retain the lowest flexure strength obtained at room temperature with 65 MPa for the assessment of the thermomechanical stress levels and their safety margins. The low tensile strength values given by the manufacturer should be considered carefully, as graphite is too brittle to be suitable for conventional tensile tests.

Table 2.1

Graphite Grade SGL R6650 :

Nonlinear thermal properties as used in the FEM calculations for the central column tiles (ANSYS).^a

Density	E modulus	Poisson ratio	Compressive strength
1870	13.5e+09	0.25	150e+06

T_pe	alpha_pe	sigtenst_pe	sigflex_t_pe	c_p	lambda_pe	emi	a	Rs
200	2.66e-06	3.66e+07	6.43e+07	178	93.5	0.7316	2.81e-04	1342
430	3.20e-06	2.89e+07	6.61e+07	1000	68.6	0.7316	3.67e-05	1147
600	3.57e-06	2.60e+07	6.74e+07	1394	57.9	0.7316	2.22e-05	1050
700	3.75e-06	2.53e+07	6.83e+07	1524	53.5	0.7316	1.88e-05	1011
800	3.91e-06	2.52e+07	6.92e+07	1633	50.2	0.7316	1.64e-05	983
900	4.05e-06	2.58e+07	7.02e+07	1729	47.5	0.7316	1.47e-05	963
1050	4.22e-06	2.76e+07	7.19e+07	1830	44.4	0.7316	1.30e-05	946
1200	4.36e-06	3.05e+07	7.38e+07	1901	41.9	0.7316	1.18e-05	940
1350	4.48e-06	3.42e+07	7.60e+07	1953	39.7	0.7316	1.09e-05	942
1500	4.59e-06	3.86e+07	7.85e+07	1993	37.8	0.7408	1.01e-05	950
1700	4.75e-06	4.52e+07	8.26e+07	2035	35.6	0.7895	9.36e-06	967
1900	4.90e-06	5.21e+07	8.75e+07	2068	34.0	0.8079	8.80e-06	993
2150	5.07e-06	6.07e+07	9.50e+07	2100	32.8	0.8342	8.36e-06	1042
2400	5.20e-06	6.83e+07	1.04e+08	2124	31.7	0.8590	7.97e-06	1113

a. All data 'conditioning' is done through the Matlab code *SGL_G.M* (see table 6.1).

3 Analytical solutions for heat conduction and thermal stress in an idealized solid

The analytical solutions provided in this chapter constitute the basis for the design considerations and design principles of the graphite tiles. Although expected temperature distributions and thermal stresses occurring in the actual tiles can be estimated by numerical methods only, the analytical calculations give guide lines and set the limits for temperatures and stresses which in return allow for validation of the results obtained with the finite element code.

Where not otherwise mentioned the planar geometry of the tile is approximated by a plate of finite thickness and infinite extension. The plasma-tile interaction is considered to be equivalent to a constant heat influx at one surface with no volume source, as the surface layer or depth in which the non-nuclear energy is deposited is small compared with the temperature penetration by thermal diffusion [ref. 13 : fig. 6]. Radiative and conductive heat flows are small for short time periods, they are calculated separately.

Thermophysical properties are averaged over the temperature range of interest (generally 293 to 2400 K) as presented earlier and calculated with the use of (equ. 2.2).

3.1 Temperature distribution

3.1.1 Solid bounded by two parallel planes

As there is no analytical solution to the differential equation of thermal conduction with temperature dependant material properties,

$$\rho c_p \frac{\partial T}{\partial t} = \text{div}(\lambda \text{grad} T) + Q$$

the following linear solutions based on the Laplace transformation [ref. 4 : p. 310 and p. 112] is used to compare the temperature distribution through a plate :

$$\begin{aligned} T_{(t,x)} - T_{(t=0)} &= \frac{q}{\lambda c} \cdot \left(\frac{1}{2} a t + \frac{1}{4} x^2 - \frac{1}{3} c^2 - \left(\frac{2c}{\pi} \right)^2 \sum_{n=1}^{\infty} \left[\frac{(-1)^n}{n^2} \cdot e^{-\frac{n^2 \pi^2 a t}{4c^2}} \cdot \cos n \pi \frac{x}{2c} \right] \right) \\ &= \frac{2q \sqrt{a \cdot t}}{\lambda} \cdot \sum_{n=0}^{\infty} \left[\text{ierfc} \left(\frac{(2n+1)c - x/2}{\sqrt{a \cdot t}} \right) + \text{ierfc} \left(\frac{(2n+1)c + x/2}{\sqrt{a \cdot t}} \right) \right] \end{aligned} \quad (\text{Equ. 3.1})$$

The plate is defined as the finite region $0 < x < 2c$, with a zero initial temperature and no flow of heat at $x = 0$ ('adiabatic plate'). Radiation is absent. There is a constant flux of heat q [W/m²] into the solid at $x = 2c$ for $t > 0$.

The temperature increase and distribution versus time over a representative plate thickness of 10 mm (thin side of the tile) is represented in figure 3.1 for a typical heat flux of 20 MW/m². Material property values are determined by averaging from the table 2.1 using (equ. 2.2) over a temperature interval from 273 to 2000 K. The temperature increase of the plate 'back side' will be less than 500 K during a typical discharge, while the exposed surface quickly reaches the allowable temperature limit.

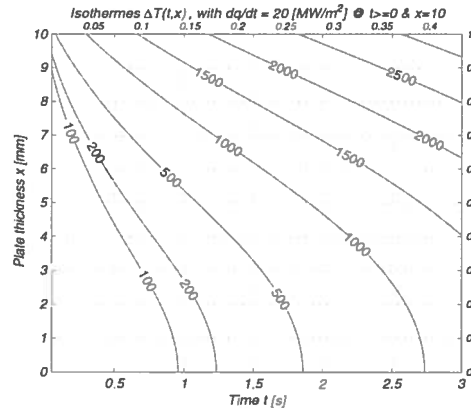


Figure 3.1

Temperature increase revealed by isothermal contour lines through a semi-infinite graphite plate heated through a constant heat influx.

As explained in [ref. 4 : p. 24] and [ref. 15 : p. 145], and in order to compare the results of this and the following chapter with [ref. 13], it is practical to express (equ. 3.1) in terms of the dimensionless variables τ (time) and ξ (position ratio), defined as

$$\begin{aligned} \tau &= \frac{a t}{4c^2} \quad \text{or} \quad t = \frac{4c^2}{a} \cdot \tau \quad \text{or} \quad 2c = \sqrt{\frac{a t}{\tau}} \\ \xi &= \frac{x}{2c} \quad \text{or} \quad x = 2c \cdot \xi \end{aligned} \quad (\text{Equ. 3.2})$$

At the front of the tile, we have $\xi = 1$, at the center $\xi = 0.5$ and at the rear $\xi = 0$. In figure 3.1, the τ graduation is the top abscissa and ξ is the right hand ordinate.

The solution (equ. 3.1) may then be rewritten as

$$T_{(t,x)} - T_{(t=0)} = \frac{2qc}{\lambda} \cdot \left(\tau + \frac{3\xi^2 - 1}{6} - \frac{2}{\pi^2} \sum_{n=1}^{\infty} \left[\frac{(-1)^n}{n^2} \cdot e^{-n^2 \pi^2 \tau} \cdot \cos n \pi \xi \right] \right) \quad (\text{Equ. 3.3})$$

The temperature is deliberately not expressed dimensionless as done in [ref. 15 : p. 207]. The physical significance of the formula is clearer if values in K (kelvin) are used. The highest temperature occurs at the end of a discharge at the exposed surface where $\xi = 1$.

3.1.2 Semi-infinite solid

For large values of t resp. τ , the surface temperature of a plate with finite thickness rises faster than the temperature on a semi-infinite solid, given by [ref. 4 : p. 75] as

$$T_{(t,x=0)} - T_{(t=0)} = \frac{2q}{\lambda} \cdot \sqrt{\frac{at}{\pi}} \quad (\text{Equ. 3.4})$$

3.2 Thermal energy balance

The thermal energy balance at the end of a load history allows to cross check the values of the thermal energy contained in the tile to the total energy influx from the plasma. A load history may be composed of just a limited time exposure or of several load and decay cycles of variable time periods.

Although there is no simple analytical solution for any temperature distribution at a specified time, the cumulated energy can be calculated semi-analytically at any temperature when the temperature gradients within the tile have flattened. The FEM calculation shows that the stationary thermal equilibrium is reached 300 to 400 s after the last heat influx and without losses.

The mass ratio of the FEM model to the geometric model is better than 0.999. Volume discretisation errors are therefore negligible. One graphite tile has a typical mass of 500 to 600 g.

By comparing the energy content at thermal equilibrium relative to the energy at initial room temperature with the energy actually contained in the tile, the radiated and conducted fractions in the energy balance can be calculated (equ. 4.6).

In the worst case scenario, each of the 32 tiles on the circumference absorbs theoretically 31250 J during a 2 s discharge at $P_{sol} = 1$ MW. Surface integration as described [chap. 4.4.1] over the FEM model produces an absorption of 33 kJ, resulting in a total discretization error of + 6 %.

3.2.1 Energy contained in a tile

If there is no energy flux leaving the tile (of negative value), the total heatflux (W/m^2) integrated over the exposed surface and over time is to be equal to the increase in thermal energy stored in the tile. The accuracy of the FEM calculation is determined by the energy values found semi-analytically and those found by FEM.

As figure 2.1B sets in evidence, the thermal capacity (or specific heat) of graphite increases non linearly with temperature. At a given temperature T , for a small temperature raise dT , the thermal energy contained in a volume fraction of mass m increases by

$$dE = m \cdot c_{p(T)} dT \quad (\text{Equ. 3.5})$$

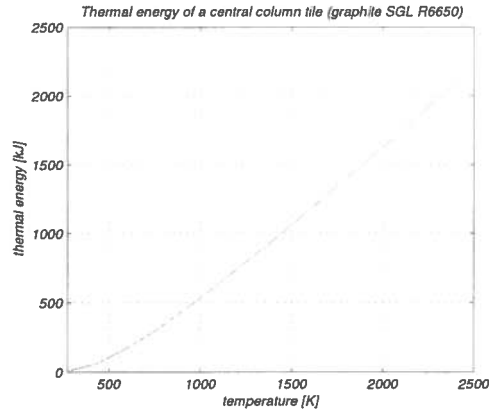
Integrating (equ. 3.5) over the total temperature raise leads to

$$\int_{E_0}^E dE = m \cdot \int_{T_0}^T c_{p(T)} dT \quad (\text{Equ. 3.6})$$

After substitution of (equ. 2.6) into (equ. 3.6) we obtain

$$E - E_0 = m \cdot \left(\frac{1}{6} a \cdot T^6 + \frac{1}{5} b \cdot T^5 + \frac{1}{4} c \cdot T^4 + \frac{1}{3} d \cdot T^3 + \frac{1}{2} e \cdot T^2 + fT \right) \Big|_{T_0}^T \quad (\text{Equ. 3.7})$$

The total thermal energy in a complete tile at a constant and uniform temperature is obtained with the use of (equ. 3.7) and plotted and listed in figure 3.2.



Temperature (K)	Energy (kJ)
293	0
* 430	61 *
600	174
700	255
800	343
900	436
1050	584
1200	739
1350	899
1500	1063
1700	1286
1900	1514
2150	1802
2400	2094

Figure 3.2
Thermal energies versus temperature in a standard central column tile (without holes or slots).

3.2.2 Radiation losses

In the particular case where the radiating tile area at temperature T_I is much smaller than the surrounding radiation absorbing area at temperature T_0 , the heat flow per unit area is [ref. 17 : Ka5] :

$$q = \sigma \epsilon \cdot (T_I^4 - T_0^4) \quad (\text{Equ. 3.8})$$

For graphite the emissivity is admittedly ~ 0.75 . As shown with the next figure, the radiation effect during a discharge accounts for a few percents of the plasma heat influx. During the pauses between discharges, radiation contributes effectively to cooling the tiles. See [ref. 14] for more details.

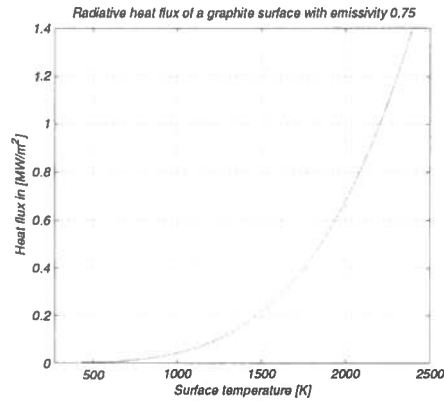


Figure 3.3
The radiative heat flux of a graphite surface is negligible during cyclical discharges, but radiative cooling is important between discharges.

For example, a graphite surface of approximately the size of the tile side facing the plasma (120 x 172 mm) would radiate 45 W/tile at 200 K above room temperature (absolute temperature 493 K) and 552 W/tile at 600 K above room temperature.

One may determine the bulk temperature decrease of a tile due to radiation, by admitting that temperature gradients are negligible and a uniform temperature distribution in the tile prevails. From (equ. 3.8), the rate at which the tile loses heat by radiation is

$$m \cdot c_p \frac{dT}{dt} = -(\sigma \epsilon A \cdot T^4)$$

Integrating from the initial temperature T_i above room temperature at time zero, we get

$$\int_{T_i}^T \frac{1}{T^4} dT = \int_0^t \frac{\sigma \epsilon A}{m c_p} dt \quad \text{and finally} \quad T_{(t)} = \frac{1}{\left(\frac{1}{T_i^3} + \frac{3 \sigma \epsilon A}{m c_p} t \right)^{1/3}}$$

Introducing the numerical and averaged values given before in this chapter and assuming a radiation time period of 600 s (10 minutes), a tile at 400 K above room temperature will have lost some 7 % of its initial energy. At 200 K a.r.t., this value is reduced to merely 1 %.

3.2.3 Conduction losses

The tile fixed on the rail inside the vacuum vessel can be seen as a block with a uniform temperature distribution, losing heat by contact through a steel slab, of which the open opposite face is the heat sink at constant room temperature (the vacuum vessel). This simplification is acceptable by recalling that the thermal conductivity of graphite is 3 to 5 times higher than steel. Introducing the relevant values into the expression $dq^* = \lambda \cdot A/s \cdot dT$, where the thermal conductivity of stainless steel is $\lambda = 15$ W/mK and A/s is the ratio of contact surface to conducting length, thermal energy losses of $q^* = 5.7$ to 8.6 W/K per tile are found. These values are based on the assumption that the contact area is equal to the actual thermally conducting surface between rail and tile. The real contact can be as low as 10 % of the geometric surface, depending on the straightness and rugosity of the surfaces. As before, the rate at which the tile loses heat by conduction is

$$m \cdot c_p \frac{dT}{dt} = q^* T$$

Integrating from the initial temperature T_i above room temperature at time zero, we get

$$\int_{T_i}^T \frac{1}{T} dT = \int_0^t \frac{q^*}{m c_p} dt \quad \text{and finally} \quad T_{(t)} = T_i \cdot e^{\frac{q^* t}{m c_p}}$$

By introducing the numerical and averaged values given before in this chapter and assuming a conduction time period of 600 s (10 minutes), a tile at any temperature will have lost up to 30 % of its initial energy.

3.3 Thermal stress and strain

The following developments apply only to a plain stress and plain strain (two dimensional) model in an orthogonal cartesian coordinate system, where the x-axis is perpendicular to the boundary plane exposed to the heat influx. Out of plane stress is zero. It is the heating condition encountered when a plate, initially at zero temperature, is suddenly exposed to a uniform ambient temperature through a boundary conductance. Assuming an infinite Biot number $B = (h \cdot 2c)/\lambda$ (or an infinite boundary conductance h , see [ref. 3]) and by rewriting (equ. 2.12), the highest theoretically possible stress (compressive when surface is shock heated) occurs at $t = 0$ at the exposed surface and is

$$\sigma_y = \sigma_z = \frac{-\alpha E \cdot \Delta T}{1 - \nu} \quad \sigma_x = 0$$

In the worst case, with 1600 K, a value of ~ 130 MPa is found. This is the upper limit for meaningful stress estimation.

A more realistic analytic approximation of stress levels through the tile is obtained by applying, from [ref. 5] and [ref. 15] :

$$\sigma_{y(t,x)} = \sigma_{z(t,x)} = \frac{\alpha E}{1 - \nu} \left[-T_{(t,x)} + \frac{1}{2c} \int_0^{2c} T_{(t,x)} dx + \frac{3(x-c)}{2c^3} \int_0^{2c} T_{(t,x)} (x-c) dx \right] \quad (\text{Equ. 3.9})$$

where the tile thickness extends again from $x = 0$ to $x = 2c$, with the half tile thickness c . From (equ. 3.9) thermal stresses in the tile over time are calculated, if the temperature distribution $T_{(t,x)}$ from (equ. 3.1) over the thickness of the tile is known. Initial relative temperature is zero. There is no prestressing ($\sigma_{y(t=0,x)} = \sigma_{z(t=0,x)} = 0$) and the plate is simply supported and can freely expand (and bend).

The attempts to solve (equ. 3.9) with *Matlab 5* by numerical integration over temperature obtained by (equ. 3.1), resp. (equ. 3.3), have failed to produce correct results. This subject needs further investigation as no explanation has been found at this point.

The following stress equation from [ref. 16] is practical and produces correct results for a temperature distribution calculated with (equ. 3.3). The dimensionless variables according to (equ. 3.2) are used. Similiar developments based on the same equations are found in [ref. 12] and [ref. 13].

$$\begin{aligned} \sigma_{y(t,x)} &= \sigma_{z(t,x)} \\ &= \frac{2qc \cdot \alpha E}{\lambda(1-\nu)} \left(\frac{\xi}{2}(1-\xi) - \frac{1}{12} + \frac{2}{\pi^2} \sum_{n=1}^{\infty} \left[\frac{(-1)^n}{n^2} \cdot e^{-n^2 \pi^2 \tau} \cdot \left(\cos n \pi \xi - \frac{12 \left(\xi - \frac{1}{2} \right) ((-1)^n - 1)}{n^2 \pi^2} \right) \right] \right) \end{aligned} \quad (\text{Equ. 3.10})$$

In the case of a tile with 10 mm average thickness, the maximum compressive stress is reached in the exposed surface after approximately 0.4 s ($\tau = 0.0506$), while highest tensile stresses occurring in the mid plane of the tile appear after 0.8 s ($\tau > 0.13$). It is important to note that these times depend on the thermal diffusivity and the tile thickness, but neither on the amount nor the rate of heat absorbed. A steady state in terms of stress and strain is reached after 3 s ($\tau > 0.45$). The values indicated for τ can be used to calculate the stress in a plate of any thickness and/or material versus time based on the definitions in (equ. 3.2)

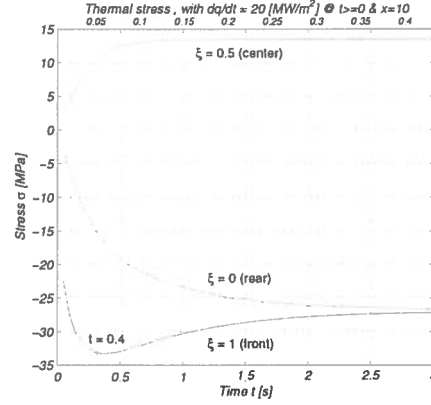


Figure 3.4

Thermal stresses in a plate according to the temperature distribution resulting from (equ. 3.1). Stresses on the front and the rear side are compressive, while the center is under tensile stress.

3.4 Optimizing the tile thickness versus permissible heat load

The heat load is limited by the maximum permissible temperature at the exposed surface and the maximum permissible thermal stress. The surface temperature should not exceed 2400 K, according to [ref. 13], and the maximum flexure stress should be below 65 MPa. The first criteria would call for a large tile thickness in order to increase inertial cooling and the second criteria would be best met with a reduced thickness minimizing thermal gradients. Inertial cooling is relevant both during a discharge and between discharges, while radiation and wall conduction contributes only between discharges [chap. 3.2.2].

Failure due to fatigue and crack propagation mechanisms is not taken into account. Combined with chemical erosion and sputtering, such cracks are usually initiated at the exposed surface. For tolerable surface defects, see (equ. 2.10). The outstanding thermoshock resistance of graphite (equ. 2.12) explains why with the chosen tile thicknesses the permissible heat load is limited by the surface temperature rather than by thermal stress. Generally a plane and relatively thin geometry without abrupt discontinuities will result in lower thermal stress. Small tiles of the characteristic size of the exponential power deposition profile and free to expand are preferred over large constrained plates. A further benefice of small tiles is that they are practically unaffected by strains occurring within the vacuum vessel walls and their support structures. In the simple cases presented hereafter with constant material properties, the allowable heat flux is likely to be limited by the compressive surface strength of graphite.

3.4.1 Heat flow limited by temperature

By imposing a temperature limit on the graphite and a permissible temperature increase, which depends on the initial temperature, the heat flux should not exceed

$$q_{\text{lim}} = \frac{\Delta T_{\text{lim}} \cdot \lambda}{2c} \cdot \frac{1}{\tau + \frac{1}{3} - \frac{2}{\pi^2} \sum_{n=1}^{\infty} \left[\frac{1}{n^2} \cdot e^{-n^2 \pi^2 \tau} \right]} \quad (\text{Equ. 3.11})$$

This expression is obtained from (equ. 3.3), with $\xi = 1$ at the surface.

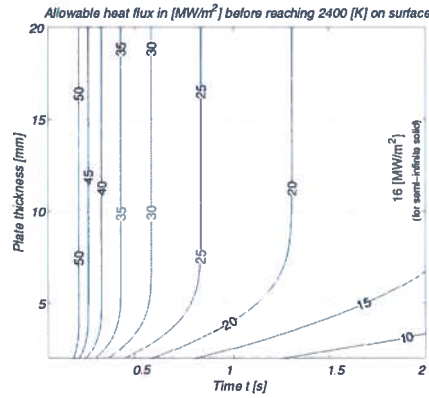


Figure 3.5

A tile of 10 mm thickness initially at room temperature, exposed to a heat flux of 20 MW/m², reaches a surface temperature of 2400 K in less than 1.4 s. The 20 MW/m² contour shows that an increase in tile thickness will not improve 'inertial cooling' (the contour line turns vertical). Another example : a tile of at least 5 mm would survive a 30 MW/m² discharge lasting no longer than 0.6 s.

3.4.2 Heat flow limited by thermal stress

From figure 2.2B, it is seen that the ratio between flexure and compressive strength of graphite is $65/150 \equiv 0.44$ at room temperature. Actual stresses in the plate exceed the ratio of 0.41 at any time. The analytically calculated stresses are principal stresses, that is, there are no shear stresses in planes perpendicular to the axes in the given particular cartesian coordinate system. It is therefore acceptable to determine the allowable heat flux from (equ. 3.10) either in terms of compressive stress at the exposed surface $\xi = 1$, figure 3.6A,

$$q_{\text{lim compressive}} = \frac{\sigma_{\text{lim compressive}} \cdot \lambda(1-\nu)}{2c \cdot \alpha E} \cdot \frac{1}{-\frac{1}{12} + \frac{2}{\pi^2} \sum_{n=1}^{\infty} \left[\frac{(-1)^n}{n^2} \cdot e^{-n^2 \pi^2 \tau} \cdot \left((-1)^n - \frac{6((-1)^n - 1)}{n^2 \pi^2} \right) \right]} \quad (\text{Equ. 3.12})$$

or in terms of flexure (or tensile) stress, in the mid plane of the tile, where $\xi = 0.5$, figure 3.6B,

$$q_{\text{lim tensile}} = \frac{\sigma_{\text{lim tensile}} \cdot \lambda(1-\nu)}{2c \cdot \alpha E} \cdot \frac{1}{\frac{1}{24} + \frac{2}{\pi^2} \sum_{n=1}^{\infty} \left[\frac{(-1)^n}{n^2} \cdot e^{-n^2 \pi^2 \tau} \cdot \cos \frac{n\pi}{2} \right]} \quad (\text{Equ. 3.13})$$

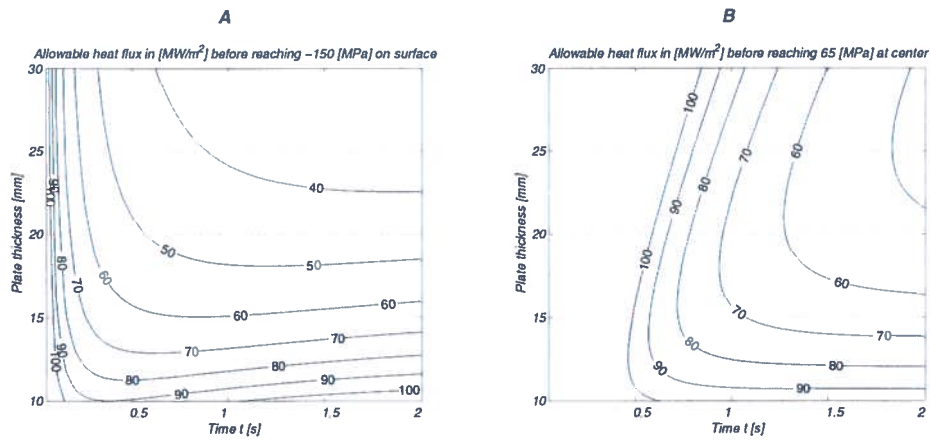


Figure 3.6

For the chosen tile thickness values, the heat flows limited by admissible stresses are much higher than those limited by temperature. These graphs apply for the semi-infinite solid only, with very limited use for 'real world cases'.

4 Finite element analysis

The present finite element analysis consists of five essential parts :

- a geometric description of the tile, which is in this case is completely parametric. Geometrically similar tiles can be modeled with an optimized element mesh for each load case;
- the definition of material properties;
- the thermal solution;
- the stress and strain solution;
- the extraction and presentation of relevant results.

All self written code files have been programed and tested to work with release 5.4 of Ansys© and are *not compatible* with any *earlier release* as lately introduced and version specific solver options have been integrated in those files. File I/O command options have considerable changed too.

4.1 Summary on mechanical design and installation of the central column tiles in TCV

The interested reader will find detailed descriptions of the tile design features in [ref. 11 : chapter 5] and [ref. 21].

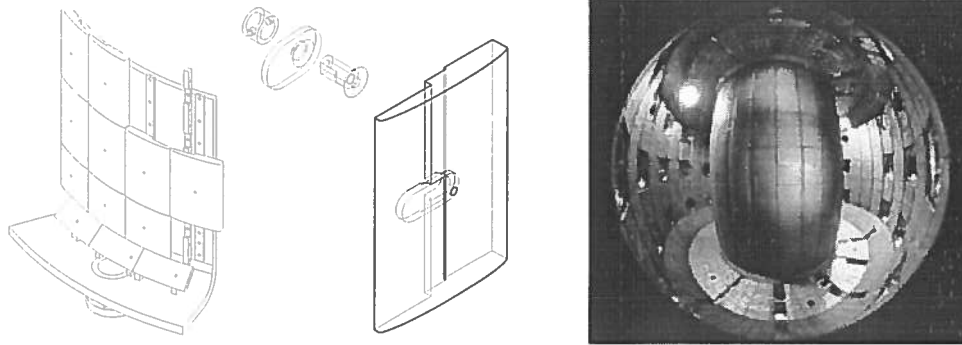


Figure 4.1

Illustrations of how the new tiles cover the vacuum vessel central column and how individual tiles are fastened torails welded to the vessel using a simple spring-free assembly comprising : a stainless steel tube for thermal expansion compensation at high temperatures, a stainless steel plate for reducing local stress on the graphite tile, a hollow Nimonic fixing screw.

4.2 Geometric description and parametric modeling of the tile cross section

In order to allow all model parameters to be modifiable and for use in future similar models, special emphasis is put on the establishment of a truly parametric model. Therefore and whenever possible, mapped meshing forced to quadrilateral elements is preferred to free meshing with mixed element shapes.

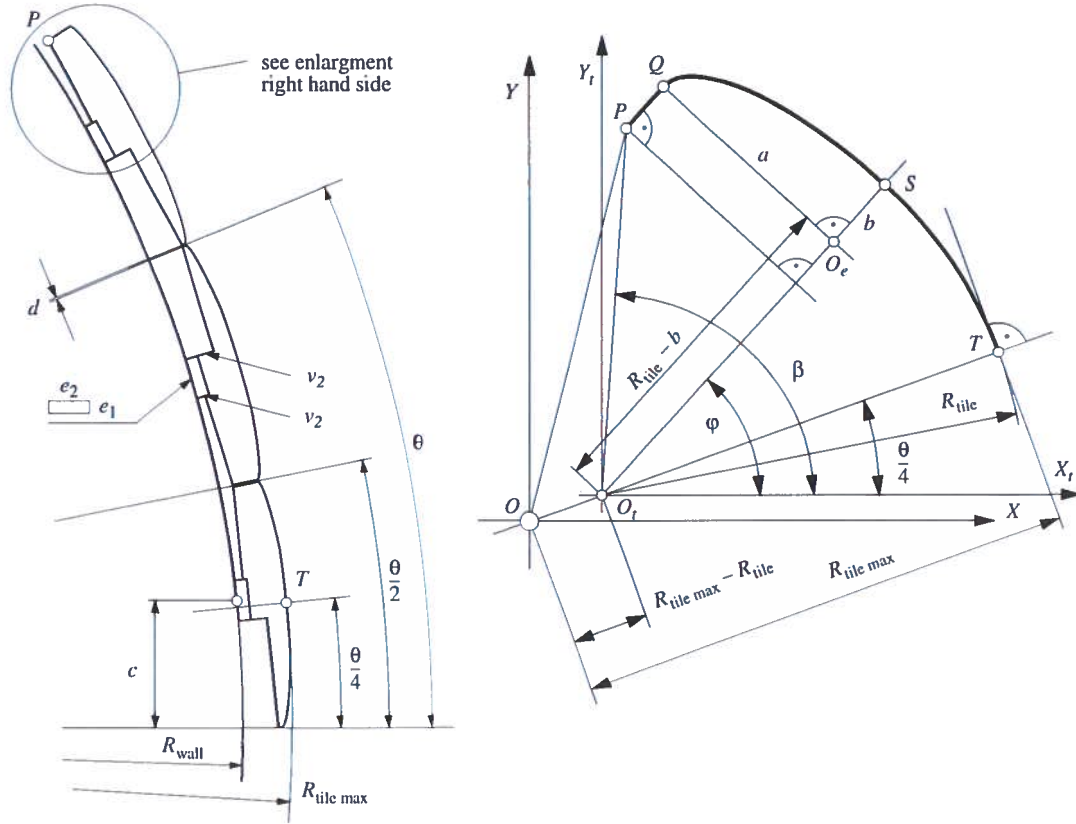


Figure 4.2

Tile alignment and geometry for the tile extending from 0° to $\theta/2 = 11.25^\circ$.

The geometric parameters introduced are :

R_{wall}	wall curvature radius on vacuum side
$R_{\text{tile max}}$	maximum radius of tile
c	rail reference distance from toroidal symmetry axis
e_1, e_2	height and width of rail (radial and toroidal extension)
θ	toroidal periodicity (symmetry axis)
R_{tile}	tile curvature radius on plasma side
d	minimum gap between tiles (toroidal)
v_1	distance from rail of tile bottom surface
v_2	distance from tile bottom surface of coil cavity
a, b	elliptic coordinates of symmetric edges
w_{tile}	width of tile (poloidal extension)

As shown in figure 4.2, the basic tile layout is determined by the toroidal periodicity $\theta = 22.5^\circ$ of the pairwise symmetric mounting rail pattern inside the vacuum chamber. Each rail, at its center line against the wall, is distant by c from the symmetry axis located at angle $n \cdot \theta$, with $n = 1 \dots 16$.

The radii of the wall R_{wall} and the outer tile surface $R_{\text{tile max}}$, i.e. the radially most distant poloidal line from the machine center and located in T , have values fixed by the geometric constraints of the plasma and the vacuum vessel.

The "inner" corner points P are obtained by intersecting one of the two parallel lines at a distance d of each other and centered at $2n \cdot \theta/2$ with the back side lines of a tile, admitted not to be direct optimization parameters. Note : these geometric separation lines are not parallel to the minor ellipse axis b . In order to simplify the formulation of boundary conditions, the tile surface exposed to the plasma is considered symmetric to its center line through T , which is the tile curvature vector R_{tile} at $2n \cdot \theta/4$ and centered in O_t . This condition implies that the toroidal gap between tiles above magnetic probes is larger than between thick ends by a small value of a few hundreds of a mm.

It is important to guarantee geometric continuity (smoothness without edges) on the surface exposed to the plasma in order to avoid "hot spots" and stress concentrations. For programmability of the machining process the middle cylindric segment is chamfered by elliptic edges, the outer contour is continuous in it's derivate (common tangent).

Assuming that the elliptic coordinates a and b have determined values within reasonable geometric limits, the angle β is calculated relative to the local cartesian coordinate system with it's origin in O_I . The angle φ is calculated by using the geometric properties of the quarter ellipse and the continuity along the cylindrically curved profile R_{tile} . Then $(R_{tile} - b, \varphi)$ are the polar coordinates of the center points of the ellipses at each edge. A minus sign is used for a contour as represented, a plus sign if the "lower" reversed edge is considered.

Non trivial geometric relationships on tile contours needed to construct the tile cross section

Based on the definitions given in figure 4.2, the following relationships are established :

polar coordinates

$$\vec{OT} = \begin{bmatrix} R_{tile \max} \\ \theta/4 \end{bmatrix}$$

$$\vec{OO_I} = \begin{bmatrix} R_{tile \max} - R_{tile} \\ \theta/4 \end{bmatrix}$$

cartesian coordinates

$$\vec{OT} = R_{tile \max} \cdot \begin{bmatrix} \cos \frac{\theta}{4} \\ \sin \frac{\theta}{4} \end{bmatrix}$$

$$\vec{OO_I} = R_{tile \max} - R_{tile} \cdot \begin{bmatrix} \cos \frac{\theta}{4} \\ \sin \frac{\theta}{4} \end{bmatrix}$$

In order to accomodate the relative position tolerances of the tiles, a constant toroidal gap width d between tile edges is imposed. Depending on the curvature of the tile in the cylindrical section with R_{tile} , there are 3 cases to be considered for the accurate positioning of the tile geometry :

- I The smallest gap is located on \overline{PQ} . Therefore the angle φ_I , calculated from β , is smaller than $\theta/2$.
- II The smallest gap occurs on the elliptic segment somewhere between Q and S on point E . Then the initial $P_I = P_{II}$, and the calculated φ_{II} is larger than $\theta/2$.
- III Out of case II, a new P_{III} is to be determined from $S - Q - a - b$. In any case φ_{III} will be smaller than φ_{II} and larger than $\theta/4$.

For computing the initial value of β , only the coordinates of P obtained from the fixed tile back side geometry need to be known. The major ellipse axis a , not b , is sufficient to calculate φ .

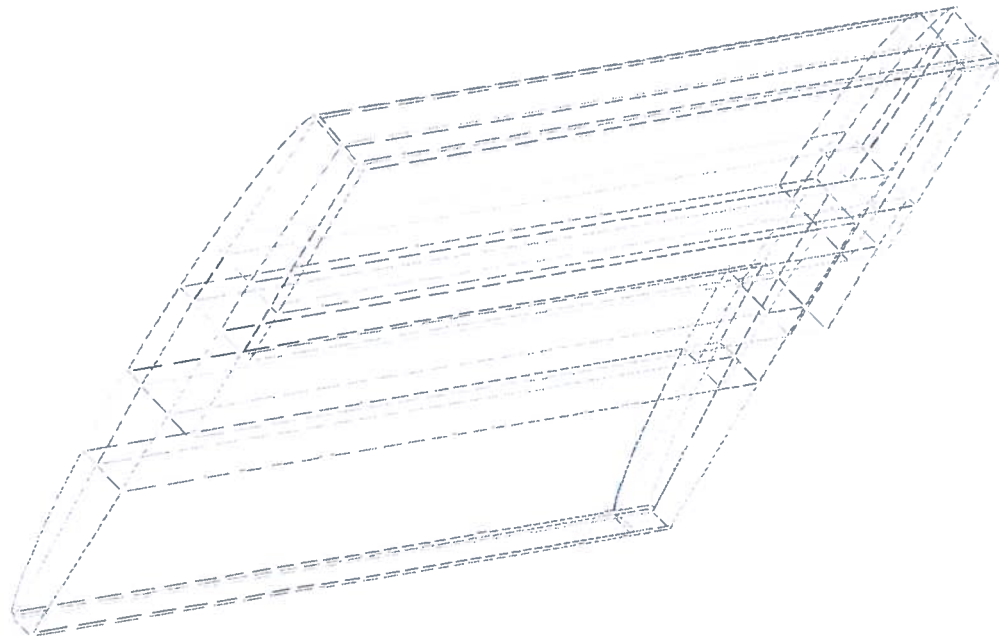
The spatial geometric properties of the ellipse are derived from the projection of the oblique intersection with a straight cylinder. For the case III, without reproducing a detailed path to solution, the point E of shortest distance between tiles and the center location of the ellipse are given as :

$$\vec{O_I E} = u \cdot \begin{bmatrix} -\sin \frac{\theta}{2} \\ \cos \frac{\theta}{2} \end{bmatrix} + \left(n - m \cdot \left(1 - \frac{b^2}{m^2} \right) \cdot \sqrt{\frac{m^2}{n^2} + 1} \right) \cdot \begin{bmatrix} \cos \frac{\theta}{2} \\ \sin \frac{\theta}{2} \end{bmatrix}$$

$$\text{where } \begin{cases} u = (R_{tile \max} - R_{tile}) \cdot \begin{bmatrix} \cos \frac{\theta}{4} \\ \sin \frac{\theta}{4} \end{bmatrix} \cdot \begin{bmatrix} -\sin \frac{\theta}{2} \\ \cos \frac{\theta}{2} \end{bmatrix} - \frac{d}{2} \\ m = \frac{-(r-b) - u/a^2 \cdot \sqrt{a^4 + r^2 a^2 - 2rba^2 - u^2 a^2 + u^2 b^2}}{1 - u^2/a^2} \\ n = \sqrt{[m + (r-b)]^2 - u^2} \end{cases}$$

$$\vec{O_I O_e} = \left[\vec{O_I H} + \vec{HG} \right] \cdot \frac{r-b}{|\vec{O_I H} + \vec{HG}|} \quad \text{where} \quad \vec{O_I H} + \vec{HG} = u \cdot \begin{bmatrix} -\sin \frac{\theta}{2} \\ \cos \frac{\theta}{2} \end{bmatrix} + n \cdot \begin{bmatrix} \cos \frac{\theta}{2} \\ \sin \frac{\theta}{2} \end{bmatrix}$$

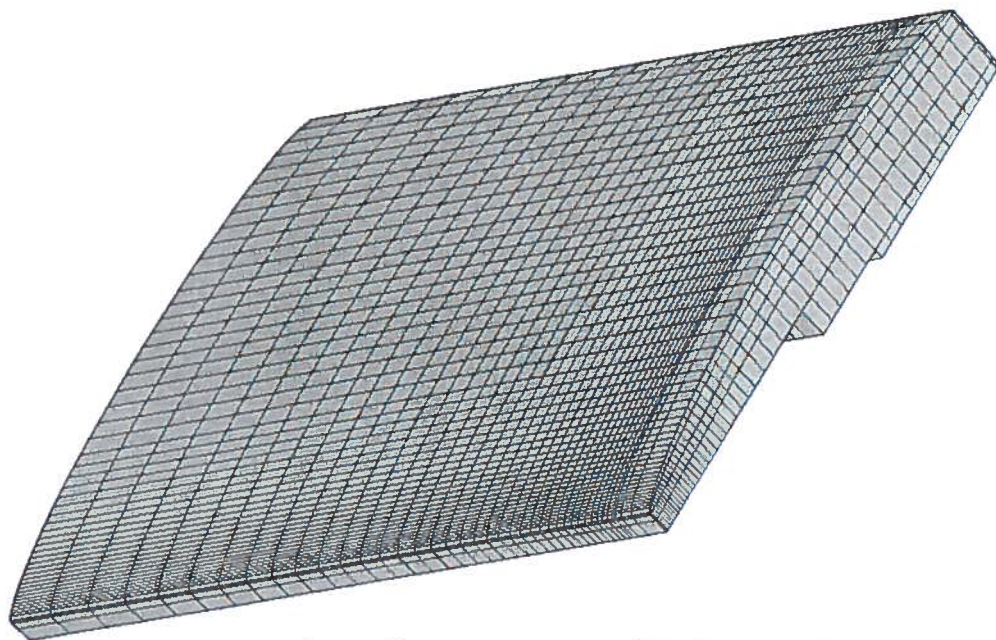
By joining all keypoints by the corresponding line segments, the complete cross-section of a tile with the rail is represented in figure 4.3.



Tile on Central Column (cc210030 / shot 11749 / 1000 kW)

Figure 4.3

This plot shows subdivided elementary volumes limited by outlines and the line divisions before meshing. Mesh is fully parametric and refinement adapts to the area of peak heat flux.



Tile on Central Column (cc210030 / shot 11749 / 1000 kW)

Figure 4.4

Tile meshed with 8-node SOLID70 elements. There are typically 12'400 nodes and 9'800 elements.

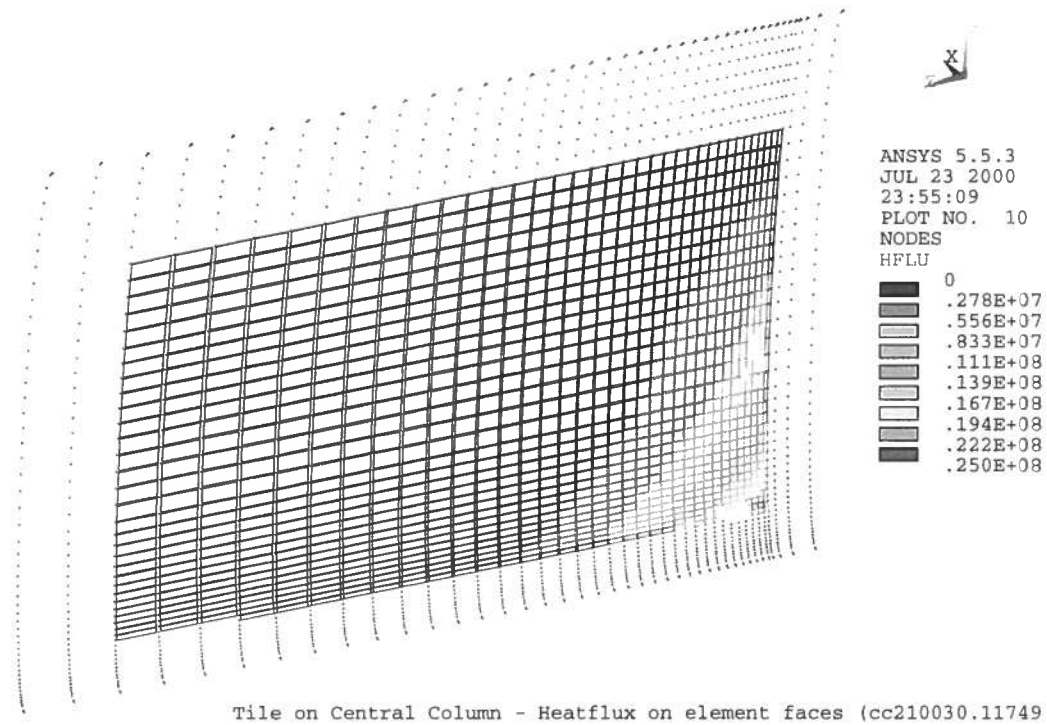


Figure 4.5

Element faces receiving heat flux at the tile surface, of which all nodes are shown.

4.3 Modelling of linear and non linear material properties

The material property flag *matprop* (located in the FILE *TILE_PAR.TXT*) offers the options of running the Ansys code either with 'linear' or with 'nonlinear' material properties which account for temperature dependant variation. In the linear case the material data is calculated from the non linear values by a table lookup for an estimated temperature entered through the constant *t_avg*. Where not explicitly mentioned, all calculations are done with non linear material properties.

As the initial time step based on the inverse thermal diffusivity calculated always at room temperature is the smallest time step actually needed, the linear properties case does not affect solver convergence behaviour [ref. 4.4.3].

In the light of the first results obtained with the inclusion of thermal radiation leading to excessively long cpu times (which has to be checked with the final code), the emissivity is admitted to be of constant value equal to 0.75, which should represent the lower limit for energy radiated from the tile.

4.4 Single and multiple discharge temperature solutions

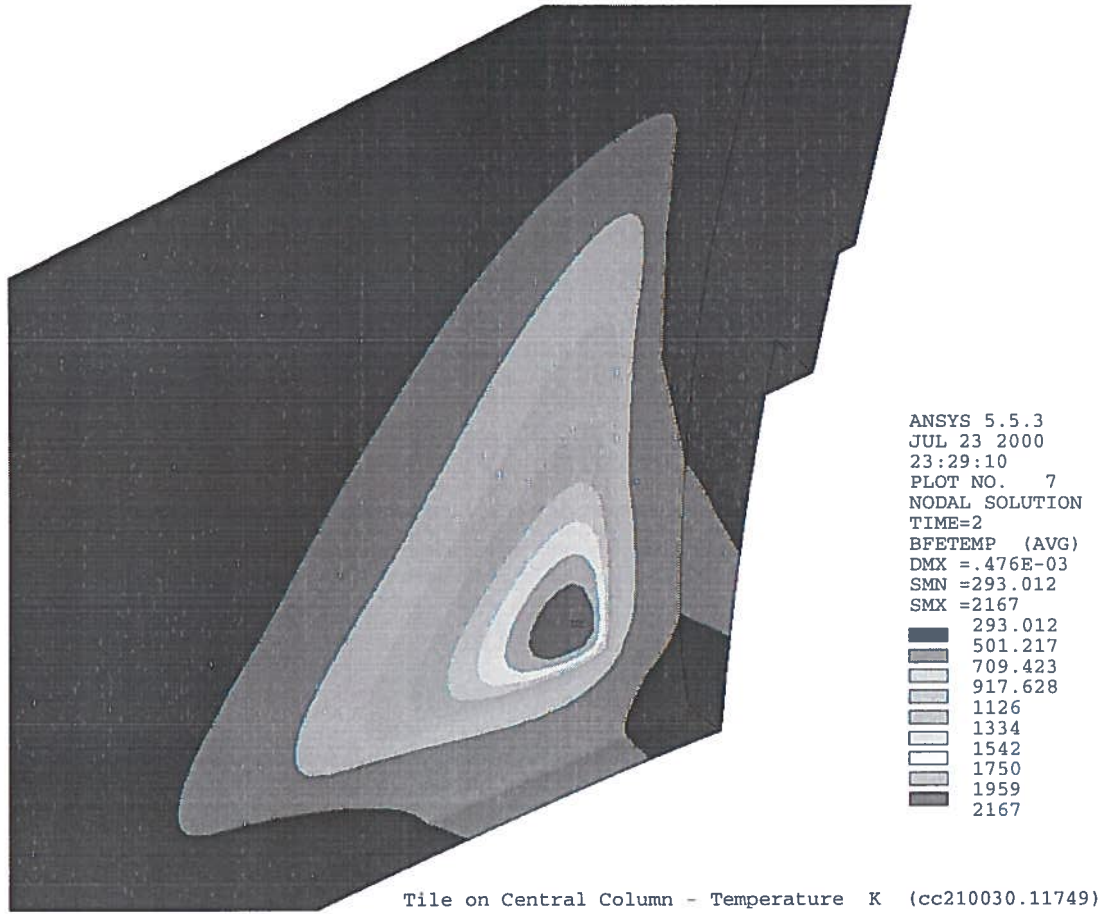


Figure 4.6

Surface temperature increasing locally where heat fluxes reach highest values. Lateral heat diffusion is negligible during plasma discharge (2 s in this case).

4.4.1 Heat influx loads and energy balance

The 'quality' of the overall FEM temperature solution is estimated by comparing 3 (+1) energy values, written into a single energy matrix (of dimension 4 x 2) :

- the theoretical energy received from the plasma, based on the plasma edge model for λ_p , see [ref. 11];
- the energy received as heat influx read from the nodal heat flux matrix (obtained from the Matlab nodal heat flux file);
- the thermal energy stored in the tile at the end of the load history, whereby radiative and conductive losses are accounted for.

The theoretical energy calculation is self-explaining :

$$E_{(1,1)} = \frac{P_{sol}/2}{n_{tiles}} \cdot t_{discharge} \cdot n_{discharges} \quad (Equ. 4.1)$$

The energy received as heat flux across the exposed surfaces is obtained by extraction of the *HFLXAVG* through the *etable* command using the *Sequence Number* method on the element face of choice. The 3D thermal solid *SOLID70* [ref. 7 online] offers the possibility to read this value for each element face separately. As all element coordinate systems are defined parallel to the global cartesian coordinate system (*KEYOPT,4,0*), the heat flows across element face 2¹. Added to that, no specific element selection is needed, since only heat flux rates caused by input heat flux are extracted. To sum up, the following operations are performed in *TILE_S.TXT*, after cycling through the complete load history :

$$E_{(2,1)} = t_{discharge} \cdot n_{discharges} \cdot \sum_{e=1}^{\text{total number of elements}} (AREA_e \cdot HFLXAVG_e) \Big|_{\text{on element face 2}} \quad (Equ. 4.2)$$

¹. While writing this paper, the author updated to the latest release 5.4 of Ansys. It appeared that element faces are no longer oriented in a foreseeable direction. The energy has now to be summed over all element faces. This does not affect the results, because faces without heat flux do not contribute to the energy balance.

The concept of calculating the thermal energy is explained earlier in this text in [chap. 3.2.1]. Let (equ. 3.7) be rewritten as the sum of energies stored in each element composing the model :

$$E_{(3,1)} = E - E_0 = \sum_{e=1}^{\text{total number of elements}} m_e \cdot \left(\frac{1}{6}a \cdot T^6 + \frac{1}{5}b \cdot T^5 + \frac{1}{4}c \cdot T^4 + \frac{1}{3}d \cdot T^3 + \frac{1}{2}e \cdot T^2 + fT \right) \Big|_{T_0}^{T_e} \quad (\text{Equ. 4.3})$$

This discrete solution is valid for any temperature distribution within the tile at any time for any model.

Relative information on energies is obtained by normalizing relative to the theoretical heat energy received [chap. 3.2] :

$$E_{(1,2)} = 1 \quad E_{(2,2)} = \frac{E_{(2,1)}}{E_{(1,1)}} \quad E_{(3,2)} = \frac{E_{(3,1)}}{E_{(1,1)}} \quad (\text{Equ. 4.4})$$

For a single discharge, by substitution of

$$n_{\text{discharges}} = 1$$

the energy equations (equ. 4.1), (equ. 4.2) and (equ. 4.3) apply.

4.4.2 Radiative and conductive boundary conditions

Because of its very low density and despite of its very high temperature, the radiated energy from the plasma to the tiles is negligible. Furthermore, the receiving surfaces are a multiple of the surface of a single belt of tiles on the central column. Additionally the plasma neither reflects nor absorbs radiated electromagnetic waves in the infrared spectrum. Consequently tile surface radiation is admitted possible not only during the idle time interval but during a discharge too. FEM results taking into account radiation show that the peak temperature at the end of a discharge decreases by approximatively 100 K at plasma power values of 500 kW and above.

There are three methods available for radiation analyses in ANSYS, each meant for different scenarios and problem dimensionalities (3D in this case). For more details on each method, see [ref. 10 : chap. 8]. Of the two approaches having been implemented, only the method applying radiation as a boundary condition through *SURF22* elements has produced useful results. Nevertheless, the second implementation will be presented at first for it's general use, since no prior knowledge of form factors or thermal radiation interchange is required.

In order to keep the FEM code as general as possible for future application, radiation might be included through the use of the *AUX12* radiation matrix generator method. The radiation matrix (see [ref. 8 : § 6.3] and [ref. 9 : § 8.1]) is calculated on the basis of the Stefan-Boltzmann law of radiation

$$Q_i = \sigma \epsilon_i \cdot F_{ij} A_i \cdot (T_i^4 - T_j^4) \quad (\text{Equ. 4.5})$$

where

Q_i	W	heat transfer rate from surface i
σ	$\text{W/m}^2\text{K}^4$	Stefan-Boltzmann constant
ϵ		effective emissivity of surface i
F_{ij}		view factor from surface i to surface j
A_i	m^2	area of surface i
T_i, T_j	K	absolute temperature at surface i and surface j, resp.

The method described in [ref. 6 : § 4.4] involves three main steps : defining the radiating surfaces, generating the radiation matrix, using the radiation matrix in the thermal analysis. The radiating surfaces are defined on the basis of the existing surface nodes where appropriate (*ESURF*) and *SHELL57* elements with temperature as a single degree of freedom. A space node is required to absorb the radiated energy. The processor *AUX12* then calculates a thermal radiation matrix, which represents radiation effects and view factors between all surfaces. There is a distinction between the *hidden* and the *non-hidden* method (see [ref. 6 : chap. 4.4]). This matrix is subsequently declared and used as a superelement *MATRIX50* in the thermal analysis. *SHELL57* are not needed further and deleted before proceeding with thermal analysis.

CPU time and file sizes are beyond reasonable limits with *AUX12* for the present tile model, so the second method based on *SURF22* surface elements is applied. All details about this element are given in [ref. 7 online]. While (equ. 4.5) equally applies, the form factor is set to 1.0, which means that there is no angular variation of the radiated energy. The outer surface of the tile is completely covered with these surface elements (*ESURF*), whereby, when heat conduction is to be included, contact surfaces to the rail in the vacuum chamber are not radiating and therefore not covered. A second material label with the emissivity is used just for the radiation boundary condition in order to exclude any unwanted cross linking to *MAT,1*. Here too, a space node, placed anywhere, is required to absorb the radiated energy. The *SURF22* are needed throughout the thermal solution and deleted after thermal solver termination only.

Radiation effects are automatically disabled when a single discharge (no cycle, no interval) is programmed (variable *mode* located in the *FILE TILE_PAR.TXT* is set to 'single').

Due to the lack of reliable experimental data quantifying the actual thermal transfer from a graphite body to a steel body, heat conduction from the tile to the vessel rail has not been implemented at this time. Therefore the control variable *conduct* located in the *FILE TILE_PAR.TXT* is set to 'no'. If available in the future, the missing data may be included with ease as the essential code bifurcations exist in the relevant program modules.

By applying (equ. 4.3) at the end of the load history, the total energy radiated and conducted to the vacuum chamber walls can be estimated as the difference of thermal energy stored in the tile to energy received as heat influx :

$$E_{(4,1)} = E_{(3,1)} - E_{(2,1)} < 0 \quad (\text{Equ. 4.6})$$

$$E_{(4,2)} = \frac{E_{(4,1)}}{E_{(1,1)}} < 0 \quad (\text{Equ. 4.7})$$

It appears, as the results will show, that the radiated energy can be rather low and that the incidence of discretization errors is not negligible, in particular after very short discharges with short decay times. In the Ansys code radiation and conduction effects are forced to 'off' when a single discharge is run.

4.4.3 Solver options and parameters

Single or multiple discharges

For a single discharge of a given duration, the value of the variable *mode* (located in the *FILE TILE_PAR.TXT*) is set to 'single'. No radiation or other effects beyond the end of a discharge are included. Basically a 'single discharge' is needed for development and test purposes only in order to reduce the time to obtain temperature results. For multiple discharges of a given identical duration, the value of the variable *mode* (located in the *FILE TILE_PAR.TXT*) is set to 'cyclic'.

The time integration parameter

The time integration parameter θ specified on the *TINTP* command relates temperature difference to temperature rate :

$$T_{n+1} - T_n = \Delta t_n \cdot (1 - \theta) \cdot \dot{T}_n + \Delta t_n \cdot \theta \cdot \dot{T}_{n+1} \quad (\text{Equ. 4.8})$$

Any value within $1/2 \leq \theta \leq 1$ is unconditionally stable. That is, all solutions are stable regardless of how large a time step Δt_n is chosen. In Ansys the default setting is $\theta = 1/2$, known as the Crank-Nicolson technique. It is usable in the majority of transient problems. For thermal shock problems with nonlinearities, a higher value to θ is recommended to avoid oscillations in time of the solution. For the case of the graphite tile, the Galerkin method was chosen with a $\theta = 2/3$. Finally the backward Euler integration scheme with $\theta = 1$ would avoid oscillations but requires finer time steps to achieve comparable accuracy. Details about the algorithm are found in [ref. 10] and [ref. 22 : p. 522].

The initial integration time step

The integration time step is the time increment used in the time integration scheme. As far as automatic time stepping or time step optimization is used, the initial value specified on the *DELTIM* command is conservative and corresponds to a dimensionless time $\tau = 1/16$, as defined previously in (equ. 2.1) and (equ. 3.2) :

$$t = \frac{4c_m^2}{a} \cdot \tau = \frac{c_m^2}{4a} = ITS \quad \text{where} \quad c_m = \text{shortest FEM length perpendicular to exposed surface} \quad (\text{Equ. 4.9})$$

A typical value for graphite used in the calculations is $ITS = 8 \cdot 10^{-3}$ s. The thickness of the first layer of elements delimiting the tile surface is approximatively $c_m = 0.8$ mm.

4.5 Thermomechanical stress solution

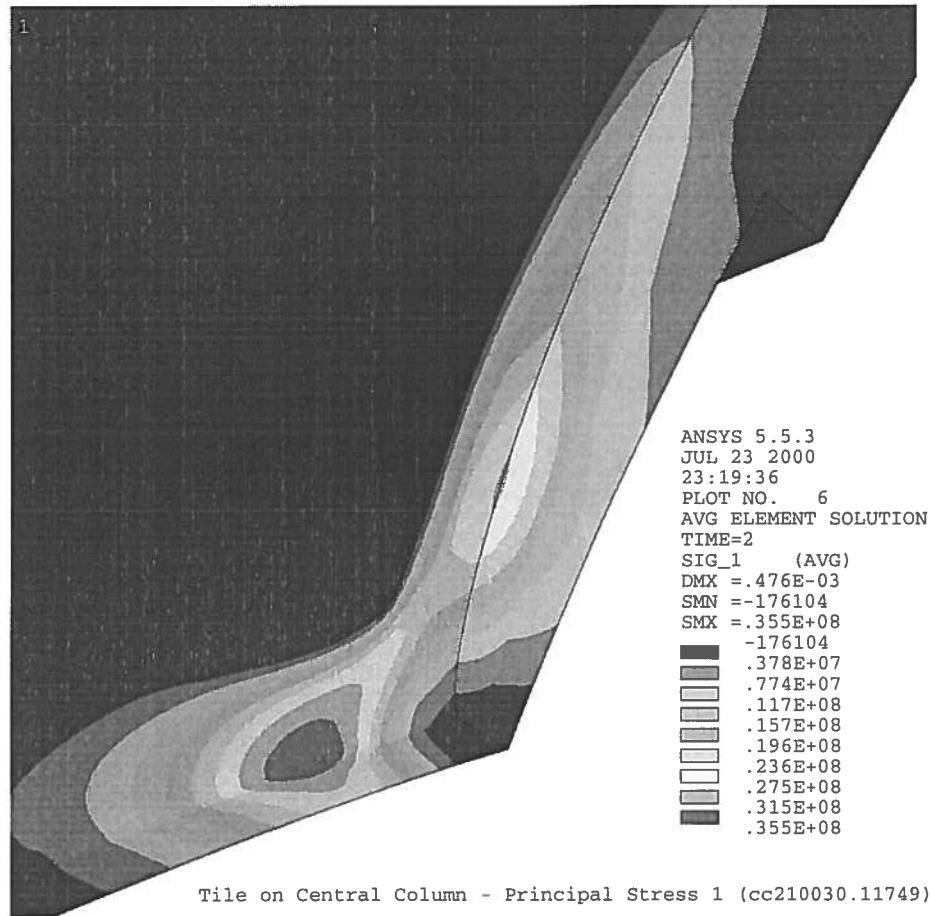


Figure 4.7

This plot mapping tensile stress reveals that the thin tile edge is subject to surface cracks, although the zones with the highest tensile stress does not coincide with the area of highest temperature.

4.5.1 Failure criteria

The spatial temperature distribution being assumed known at any given time by the results in [chap. 4.4], the problem of three dimensional, inertia free thermoelasticity consists in the determination of the following 15 equations [ref. 15] :

- 3 force-equilibrium equations (sum of all forces zero);
- 6 stress-strain relations (stress-strain and shear-rotation);
- 6 strain-displacement relations (strain-elongation and angular strain-rotation), while rigid-body motion is zero.

In any stress system, representable by an infinitesimal cube in a cartesian coordinate system, 3 mutually perpendicular planes, on which no shear stresses act, exist at each point within the heated strained solid. The normal stresses on these particular planes are called principal. One of them is the maximum stress σ_1 (greatest positive or least negative) and another is the minimum stress σ_3 (least positive or greatest negative). For example an immersed, non-absorbing body could have 3 negative principal stresses, but not necessarily of equal value (elastic compression).

Once the stress values have been computed, the 'safety margin' versus available strength data has to be assessed. The difficulty with brittle materials is to correlate a calculated three dimensional stress state with values found experimentally and usually given in terms of tensile or flexural strength only. For materials similar to graphite (concrete, ceramics among others), compressive strength is usually much higher than tensile or flexureal strength.

Several failure criteriae like VonMises or Mohr [ref. 5] are applicable for ductile-elastic material (steel, aluminium) only. But graphite 'behaves' essentially as a brittle material. Its failure mechanisms are those of ceramic materials, where statistical concepts (failure probability), defects (internal and surface, number and distribution), loading modes and amount and topology of stressed volume are relevant. Other keywords are crack propagation and crack growth. As was stated in [chap. 2], the data and resources for appropriate assessments are not available. From documented investigations in Tokamaks we know that the damaged surfaces have cracks propagating perpendicularly to the surface, a phenomena not (yet) observed in TCV. With the criteria of maximum principal stresses, failure occurs when at least one of the following conditions is reached :

$$\begin{array}{llll} \sigma_1 \geq \sigma_{\text{limit tensile}} & = 65 \text{ MPa} & = \text{tensile failure} & \text{for } \sigma_1 > \sigma_2 > \sigma_3 \\ \sigma_3 \leq \sigma_{\text{limit compressive}} & = -150 \text{ MPa} & = \text{compressive failure} & \end{array} \quad (\text{Equ. 4.10})$$

There are some more or less sophisticated failure criteria applicable for brittle materials, all derived from and expressed in terms of principal stresses (see [ref. 3] and [ref. 20]). Some have been included in the program, but their results are not documented :

- the stress intensity or the maximum of absolute values of the differences of principal stresses

$$\sigma_i = \max(|\sigma_1 - \sigma_2|, |\sigma_2 - \sigma_3|, |\sigma_3 - \sigma_1|)$$

- the arithmetic average of principal stresses or the arithmetic average of principal stresses

$$\sigma_{\text{avg}} = (\sigma_1 + \sigma_2 + \sigma_3)/3$$

- the equivalent or VonMises stress

$$\sigma_{\text{eqv}} = \sqrt{((\sigma_1 - \sigma_2)^2 + (\sigma_2 - \sigma_3)^2 + (\sigma_3 - \sigma_1)^2)/2}$$

- the Coulomb-Mohr criteria

$$\sigma_{\text{eqv CM}} = \sigma_1 - \chi \sigma_3 \quad \text{with} \quad \chi = \sigma_{\text{limit tensile}} / \sigma_{\text{limit compressive}}$$

- the Pissarenko-Lebedev criteria

$$\sigma_{\text{eqv PL}} = \chi \sigma_{\text{eqv}} + (1 - \chi) \sigma_1 A^{1 - \frac{3\sigma_{\text{eqv}}}{\sigma_{\text{eqv}}}} \quad \text{with} \quad A \approx 0.7 - 0.8 \quad \text{for brittle materials}$$

- the Kuhn criteria (based on deformation energy) might be used with some restriction, but the considerable ratio of 165/65 between compressive and tensile strengths is not predicted correctly for graphite.

$$\begin{aligned} \sigma_{\text{eqv tensile}} &= \frac{2(1+\nu)}{3} [\sigma_1^2 + \sigma_2^2 + \sigma_3^2 - (\sigma_1\sigma_2 + \sigma_2\sigma_3 + \sigma_3\sigma_1)] + \\ &\quad \frac{1-2\nu}{3} (\sigma_1 + \sigma_2 + \sigma_3) [\sigma_1^2 + \sigma_2^2 + \sigma_3^2 + 2(\sigma_1\sigma_2 + \sigma_2\sigma_3 + \sigma_3\sigma_1)]^{1/2} \\ \sigma_{\text{eqv compressive}} &= \left[\frac{3}{1+4\nu} \right]^{1/2} \cdot \sigma_{\text{eqv tensile}} \end{aligned}$$

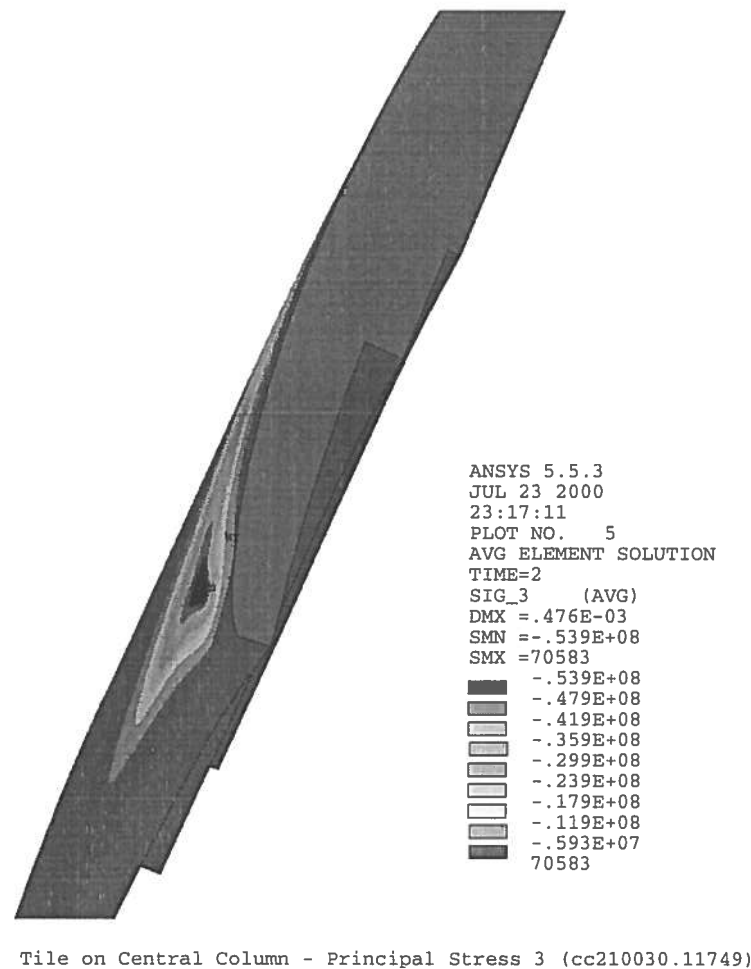


Figure 4.8

As the heated material expands, compressive stress is most severe where temperature is highest, causing non negligible curvature of the free unsupported thin side of the tile. The thick side of tile will curve less as the resisting crosssection is larger.

4.5.2 Initial temperature boundary conditions and displacement constraints

Methodology

Thermal-stress applications are treated in a so-called *coupled-field analysis*, which takes into account the interaction between thermal expansion and mechanical stress. Because in the present case strain does not influence on temperature, we are in a *one-way* coupling situation best handled by the *indirect method*, where nodal temperatures from a (time transient) thermal analysis are applied at a *specified time* in the subsequent (steady state) stress analysis. The *direct method* involving one (time transient) thermomechanical analysis with a dedicated *coupled field element* may look attractive, but is not practicable for larger models because of the huge amount of cpu time and storage space required (33'000 s to read $t = 0.224$ s with *SOLID5* elements).

Furthermore the *direct method* would require the use of the time history postprocessor *POST26* in order to determine the space & time values where & when the maximum stress occurs. In this case one would 'ask': At what time a given element reaches the highest stress (the value of which depends on the chosen criteria)? Commands offering very limited processing capabilities like *NSOL* & *ESOL* to create time dependant solution vectors have to be employed. With the *indirect method* using the static standard postprocessor *POST1* to extract results, one would 'ask': Which element has the highest stress at a given time? Results are extracted from the solution files with *ETABLE* commands, allowing straight forward computation of relevant stress functions.

We shall apply the *indirect method*, with a simple algorithm based on comparing stress results between refined adjacent time steps. Thus the variable *method* (located in the *FILE TILE_PAR.TXT*) is set to 'indirect'.

Choosing a load case

In transient thermomechanical calculations the maximum (triaxial) stress condition does not necessarily occur in the region where the thermal gradient reaches its peak value. This fact is evident by comparing temperature gradients from figure 3.1 with corresponding stress values at various time points in figure 3.4. It has been shown that stress levels are tending to be lower after the first discharge. In the present Ansys code stress is not computed when multiple or cyclic discharges are run, as the main interest in such cases is the temperature distribution.

Stresses are computed for several time steps within a discharge and then compared (unlike the results of [chap. 3.3], stresses have been found to be maximum at the end of a discharge).

Clamping to avoid rigid-body motion

Rigid body motion is not acceptable in the present model, valid for a non moving tile only. In order to avoid numeric inconsistencies, which are a consequence of the numeric integral of all forces (= stresses x surfaces) not being exactly equal to zero, the tile has to be fixed in space in such a way, that rigid body motion is excluded without inducing stresses by the 'clamping'. This is achieved by removing in three nodes belonging to one same plane all 6 degrees of freedom (translations and rotations). The stresses found with these boundary conditions represent the lower limit.

A tile with just no rigid body motion is free to expand and bend and is as such a theoretical model only. In practice however the 'real' tile is restrained to some degree from bending along the rail inside the vacuum vessel. In Ansys, while gliding along the rail is permitted, nodes are kept in contact with the rail surface. The partially suppressed expansion results in the highest possible stresses, which should be taken as the design limit values.

4.5.3 Solver options and parameters

For the reasons explained earlier, the *indirect method* has been chosen to calculate the coupling between temperature and stress/strain. An *element type change (ETCHG,TTS)* is necessary to substitute *SOLID70* (3-D 8-Node Thermal Solid) with *SOLID45* (3-D 8-Node Structural Solid) elements in order to apply nodal temperatures as thermal loads.

There are no inertial effects (mass), so the analysis type is static for each load step. In this process the time axis is used only to correlate static stress solutions with temperature distributions at specified time points. There is no direct time dependency between stress solutions as the stress at time $t-1$ does not influence stress at time $t-0.5$ and so forth.

5 Results and conclusions

The relevant results are compiled in table 5.1, subdivided on a case by case scheme. Blank fields contain no data at all.

5.1 Case list

Case T

These are the 'theoretical' results based on the analytical solutions developed in [chap. 3] :

- Constant physical graphite data is used, as detailed in [chap. 2], where the actual averaged values can be found in figure 2.1 and figure 2.2.
- Temperatures are computed with (equ. 3.1) for both the thin and the thick semi-infinite plate, with conforming heat flux values.
- There are no thermal losses (radiation or conduction).
- Thermal stresses are obtained with (equ. 3.10). The plate is free to expand and to bend.

Case A, B & C

These cases constitute the theoretical limits in regard of stresses, as the absence of radiation and conduction results in the highest possible thermal gradient through the tile.

- Obtained with Ansys as described in [chap. 4].
- Case A is based on linear averaged material properties and uniform constant heat flux on cylindric and elliptic surfaces on the thick tile side. It is presented here for cross checking only.
- B versus C shows how the fixture of the tile to the rail affects stress levels. Material properties are nonlinear.

Case D & E

More realistic time dependant temperature distributions require the inclusion of radiation effects :

- All surfaces radiate with an emissivity of 0.75, as all surrounding surfaces are likely to be at room temperature.
- Since temperature gradients are equal or lower than in A/B/C, no stresses are computed.

5.2 Discussion

Limited configurations result in higher thermal loads and higher stress levels than diverted configurations. Temperatures found in diverted cases do not exceed 1630 K (# 11749), while reaching 2160 K in a limited mode (# 12907) on a tile initially at room temperature.

By comparing the results obtained analytically (case T) with the linear, uniformly heated FEM solution (case A), a good agreement is found in the temperature values : 2'578 K (T) versus 2528 K (A). The stress levels are similar, although the FEM model predicts higher tensile stress, 36 versus 27 MPa, and lower compressive stress with - 69 versus - 74 MPa. This is in accordance with a slightly higher backside temperature of the tile in the FEM result, suggesting a higher average temperature in the tile and therefore lower tensile and higher compressive stress than in the analytical case T. Linear solutions lead in both models to overestimate temperatures, as the average diffusivity is lower than the non linear diffusivity below 1000 K.

If we compare the non linear case B with A and T, we find lower tensile stress of 21 MPa (B) and higher compressive stress - 88 MPa (B) for discharge # 12907 on the thick side. In graphite the thermal conductivity and thermal diffusivity decrease versus temperature, while the thermal expansion coefficient increases. This implies, as the non linear results show, that the temperature rises less to peak at 2160 K only and that the heated volume fraction is smaller, leading to higher near surface compression and a larger cross section under tensile stress.

With a minimum emissivity of 0.75, the temperatures induced by cyclic heat load of 25 MW/m² are expected to be below 2200 K or 1900 °C on the 'thin' tile side, if a minimum time interval of 600 s is maintained. Thermal equilibrium is reached after 5 limited discharges, as shown in figure 5.1 for the case E. The residual thermal gradients within the tile become very small : a thermal energy of 51 kJ is contained in a tile at average 403 K (from figure 3.2), while the Ansys result is 46 kJ.

The magnetic probes face graphite at a temperature of less than 570 K or 270 °C, a value which is below the baking temperature of the vacuum vessel.

Stresses in graphite should be limited to values ranging from - 150 MPa to + 65 MPa (see [chap. 2] and [chap. 4.5.1]), though the mechanical resistance tends to increase noticeably with temperature. As computed stresses never exceed 65 % of these limits (case C), temperature appears to be the restraining factor. During cyclic heating temperature gradients and thus thermally induced stresses tend to decrease. Cyclic stress limits or fatigue data are neither available and nor is there a reliable method to calculate such behaviour, which should take into account the actual and entire thermomechanical history of the graphite. Particular features at the tile surface, mainly at the edges, like grooves, cracks or sharp changes in cross section, result in stress concentration effects and have to be avoided. The edge contour of the exposed tile surface 'sees' the highest tensile stresses, while the surface area of highest heat influx shows the highest compressive stress. Elastic prestressing from the fixture system has not been included in the simulation, but its location beneath the surface has been chosen such as to be as 'far' as possible from the areas where the highest heat fluxes and highest stresses occur.

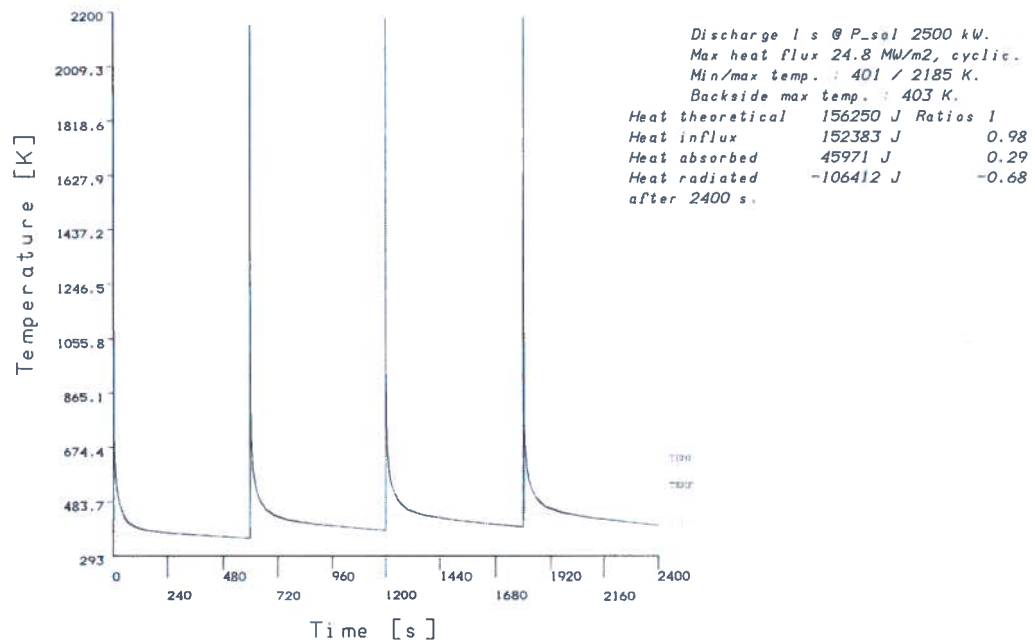


Figure 5.1

Case E: absolute temperatures of the hottest and the coolest nodes in the tile, and the hottest node potentially facing a magnitec probe ('thin' side of tile). Radiation is included. Temperatures do not increase further after 5 discharges with 600 s intervals.

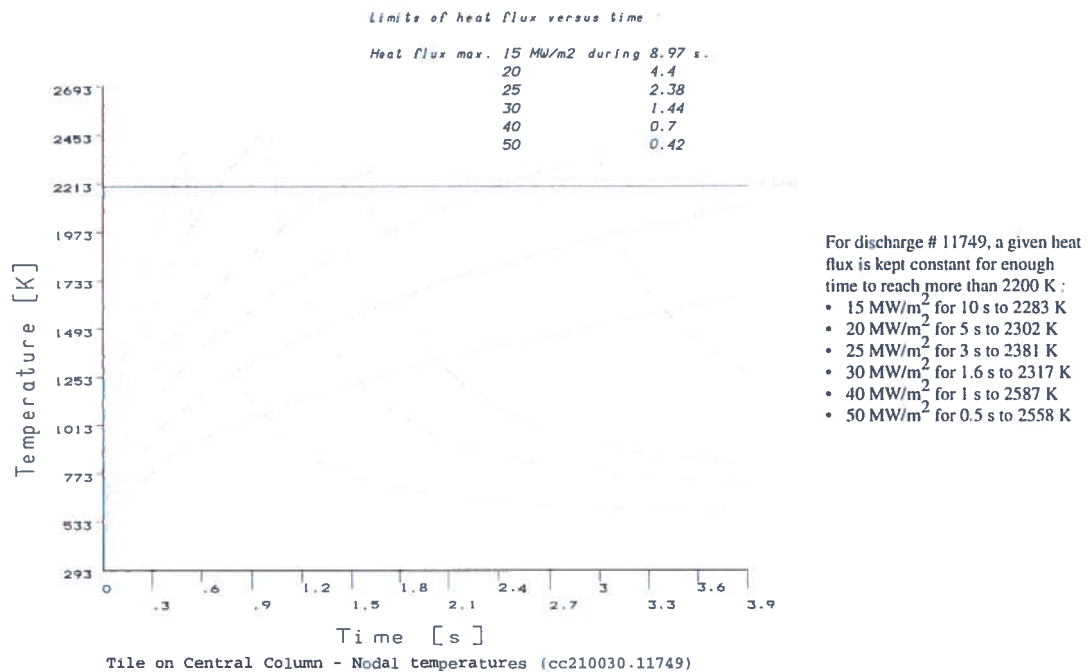


Figure 5.2

Case D: Heat flux limits versus time for diverted configurations for the highest tolerable temperature criteria, based on discharge # 11749 renormalized on various peak heat fluxes. Heating occurs on the 'thin' side (above magnetic probes) of the tile.

Table 5.1
Overview

	Chronology			Boundary conditions			Material properties		TCV Shot				
	Number of discharges	Duration per discharge	Idle time interval	Radiation	Conduction	Displacements		Linear	Non linear	# 11749		# 12907	
						6 DOF	Rail			Thick side	Thin side	Thick side	Thin side
Load case													

Configuration									diverted		limited	
P_{SOL}									1 MW		2.5 MW	
λ_q									3 mm		3 mm	
P_{max}									22.5 MW/m ²		24.8 MW/m ²	

T 1 s	1	1 s						✓		semi-infinite plate with 18 (~ thick) & 10 mm (~ thin)			
	Heat theoretical (received on area equivalent to tile surface)									464 kJ	464 kJ	512 kJ	512 kJ
	Maximum surface temperature			exposed to plasma						2'366 K	2'366 K	2'578 K	2'578 K
				backside of tile						294 K	420 K	294 K	433 K
	Stress			maximum tensile						24.8 MPa	15.3 MPa	27.3 MPa	16.9 MPa
				maximum compressive						- 67.1 MPa	- 34.1 MPa	- 74.0 MPa	- 37.6 MPa

A 1 s	1	1 s				✓		✓		uniformly distributed heat flux			
	Heat theoretical												
	Heat influx (total heat flux integrated over element faces)											282 kJ	225 kJ
	Heat in tile (thermal energy integrated over element volumes)												
	Maximum nodal temperature			exposed to plasma								2525 K	2549 K
				backside of tile (magn. probe)								309 K (319 K)	293 K (788 K)
	Stress			maximum tensile								35.8 MPa	24.6 MPa
				maximum compressive								- 69 MPa	- 76.4 MPa

B 1 s	1	1 s				✓			✓				
	Heat theoretical									15'625 J (1.00)	15'625 J (1.00)	39'063 J (1.00)	39'063 J (1.00)
	Heat influx (total heat flux integrated over element faces)									15'264 J (0.98)	15'263 J (0.98)	38'116 J (0.98)	38'096 J (0.98)
	Heat in tile (thermal energy integrated over element volumes)									15'893 J (1.02)	15'792 J (1.01)	38'788 J (0.99)	38'614 J (0.99)
	Maximum nodal temperature			exposed to plasma						1'608 K	1'630 K	2'148 K	2'160 K
				backside of tile (magn. probe)								345 K	522 K
	Stress			maximum tensile						16.3 MPa	21.6 MPa	21.3 MPa	25.9 MPa
				maximum compressive						- 44.5 MPa	-38.2 MPa	- 88.1 MPa	- 84 MPa

C 1 s	1	1 s					✓		✓				
	Heat theoretical											39'063 J (1.00)	39'063 J (1.00)
	Heat influx (total heat flux integrated over element faces)											38'116 J (0.98)	38'096 J (0.98)
	Heat absorbed (thermal energy integrated over element volumes)											38'788 J (0.99)	38'614 J (0.99)
	Maximum nodal temperature			exposed to plasma								2'148 K	2'160 K
				backside of tile (magn. probe)								345 K	522 K
	Stress			maximum tensile								24.2 MPa (0.37)	28.8 MPa (0.44)
				maximum compressive								- 99.5 MPa (0.66)	- 89.6 MPa (0.60)

Table 5.1
Overview

Load case	Chronology			Boundary conditions				Material properties		TCV Shot				
	Number of discharges	Duration per discharge	Idle time interval	Radiation	Conduction	Displacements		Linear	Non linear	# 11749		# 12907		
						6 DOF	Rail			Thick side	Thin side	Thick side	Thin side	
D 600 s	1	1 s	599 s	✓		✓			✓					
	Heat theoretical										renormalized on peak power fluxes 15 / 20 / 25 / 30 / 40 / 50 MW/m ²		39'063 J (1.00)	
	Heat influx (total heat flux integrated over element faces)										9'661 / 12'881 / 16'101 / 19'321 / 25'761 / 32'202 J		38'116 J (0.98)	
	Heat in tile (thermal energy integrated over element volumes)										6'628 / 8'723 / 10'766 / 12'755 / 16'609 / 20'305 J		24'435 J (0.63)	
	Heat radiated (heat influx minus heat in tile)										3'032 / 4'158 / 5'334 / 6'566 / 9'153 / 11'897 J		13'681 J (0.35)	
	Maximum nodal temperature				exposed to plasma						1'105 / 1'395 / 1'691 / 1'995 / 2'587 / 3'136 K		2'104 K	
					backside of tile (magn. probe)						477 / 510 / 536 / 560 / 599 / 632 K			
	Minimum nodal temperature (at end of 1 cycle ~ 10 minutes)										313 / 318 / 324 / 329 / 338 / 347 K		357 K	
E 2'400 s	4	1 s	599 s	✓		✓			✓					
	Heat theoretical												156'250 J (1.00)	
	Heat influx (total heat flux integrated over element faces)												152'383 J (0.98)	
	Heat in tile (thermal energy integrated over element volumes)												45'971 J (0.29)	
	Heat radiated (heat influx minus heat in tile)												106'412 J (0.68)	
	Maximum nodal temperature				at end of each discharge								2'116 -> 2'156 -> 2'175 -> 2'185 K (+40 +29 +10 K)	
					backside of tile (magn. probe)								564 K	
	Minimum nodal temperature in tile at end of idle time interval												356 -> 383 -> 395 -> 401 K (+27 +12 +6 K)	

6 Code file listing

Each discharge or plasma configuration is referred to by a number. For each such discharge number, $2 \times 3 \times 3 = 18$ load cases are considered to be representative for all possible cases. The load cases are encoded in a file numbering scheme, where the so called 'case id.' is concatenated of :

- *ccpcxxx/* = directory with heat flux files, where *xxx*10* stands for discharge energy in kW
- *1* = thick side / *2* = thin side of the asymmetric tile
- *010 / 086 / 130* = distance in mm from the tile edge at $z = 0$
- *25 / 50 / 75* = λ_q , the scrape off lengths of the power flux (heat) in tenths of millimeters

Load cases on the lower and upper tile edges with $z = 0$ or $z = \text{tile width}$ have not been considered and are in principle not allowed in terms of plasma configuration.

Table 6.1

Project related code files

Ansys files, located in /ho/users/chavan/projects/files/cc_tiles/ansys/

Item	Description & purpose		/Directory/Filename	Suffix	Extension
Program file	Modular command sequence & i/o file	writes nodal attributes	TILE	_A	.TXT
		main file	TILE	_B	.TXT
	Parameter file		TILE	_PAR	.TXT
	Modeling & meshing		TILE	_MOD	.TXT
	Boundary layer extraction		TILE	_LBN	.TXT
	Radiating layers		TILE	_RAD	.TXT
	Thermal solver		TILE	_S_T	.TXT
	Stress solver		TILE	_S_S	.TXT
	Postprocessing & graphics	end of load case	TILE	_PP	.TXT
		time history	TILE	_PPT	.TXT
		animation	TILE	_PPA	.TXT
		time hist case D	TILE	_PPTD	.TXT
Auxiliary program file	Mesh transition for 4 sided areas with 3 sub-regions		/MACROS/M43TRANS		.MAC
	Linear mesh transition for 4 sided areas		/MACROS/MTRANS		.MAC
	Mesh propagation depending on toroidal impact zone		MACROS/PHI_TEIL		.MAC
	Read formatted array from text file		/MACROS/MATRIX_RD		.MAC
	Write formatted array to text file		/MACROS/MATRIX_WR		.MAC
	Sort data vector based on element number vector		/MACROS/VECTSORT		.MAC
Material data base	Graphite SGL R 6650		/MATERIAL/SGL_G		.TXT
Utility file	Command sequences for creating ngf from Ansys		FIG_FOR_REP		.TXT
	Convert files .ngf to .epsi		NGF2EPSI		.TXT
	Ansys neutral graphics file		PLOTS_CC	case id.	.NGF
	EPSI file, referring to this report		/FIGURES/FIGURE_	case id.	.GRPH
	Color maps for contour plots, with the same RGB definitions as their counterparts in Matlab	bone	/COLORS/BONE		.CMAP
		gray	COLORS/GRAY		.CMAP
		pink	COLORS/PINK		.CMAP
		hsv	COLORS/HSV		.CMAP
Result file	Node numbers & coordinates for Matlab		/CC/RC_	case id.	.TXT
	Nodal heat fluxes from Matlab		/CC/RP_	case id.	.TXT
	Complete model data base		CC	case id.	.DB
	Temperature solution		CC	case id.	.RTH
	Stress & strain solution		CC	case id.	.RST

Table 6.1*Project related code files*

	Item	Description & purpose	/Directory/Filename	Suffix	Extension
Matlab	Program file	Material data & parameter file for polycrystalline graphite, Ringsdorff (SGL Carbon Group), grade R 6650	PROJECTS/MATERIALS/ CARBON/GRAPHITE/ MATLAB/SGL_G		.M
		Graphical output	PROJECTS/MATERIALS/ CARBON/GRAPHITE/ MATLAB/SGL_G_PLOTS		.M
	Utility file	Various RGB color maps for use in Ansys	CMAP_MATLAB2ANSYS		.M
	Theory	Field line mapping to calculate thermal surface loads	FIELDLINES		.M

7 References

- [1] *Technische keramische Werkstoffe*, DKG, ISBN 3-87156-091-X, 1991.
- [2] *Les céramiques thermomécaniques*, CNRS, ISBN 2-87682-021-8, 1989.
- [3] *Mechanisches Verhalten keramischer Werkstoffe*, Springer, ISBN 3-540-51508-9, 1989.
- [4] *Conduction of Heat in Solids*, Oxford Science Publications, ISBN 0 19 853368 3, 1959.
- [5] *Theory of Elasticity*, McGraw-Hill, ISBN 0-07-Y85805-5, 1987.
- [6] *ANSYS User's Manual for Rev. 5.0 - Procedures*, Volume I, DN-R300:50-1, 12.1992.
- [7] *ANSYS User's Manual for Rev. 5.0 - Elements*, Volume III, DN-R300:50-3, 12.1992.
- [8] *ANSYS User's Manual for Rev. 5.0 - Theory*, Volume IV, DN-R300:50-4, 12.1992.
- [9] *ANSYS Thermal Analysis*, Tutorial for Rev. 5.0, DN-T031:50, 6.1992.
- [10] *ANSYS Heat Transfer*, User Guide for Rev. 5.0, DN-S221:50, 6.1993.
- [11] *The Design of Central Column Protection Tiles for the TCV Tokamak*, Nuclear Fusion, Volume 39, Number 10, 1999.
- [12] *Limiter für den Stellerator W VII-AS - Zum Stand der technischen Voruntersuchungen*, MPI-IPP 2/276, 8.1985.
- [13] *Thermal Processes in Tokamaks of the the Next Generation and Future Reactors*, J. of Nuclear Materials 111 & 112, p. 531 - 540, 1982.
- [14] *Scaling laws for Thermal Behavior of Intertially Cooled Limiters Allowing for Temperature-Dependant Material Properties*, J. of Nuclear Materials 111 & 112, p. 566 - 568, 1982.
- [15] *Theory of Thermal Stresses*, Dover, ISBN 0-486-69579-4, 1997.
- [16] *Thermal Stresses*, McGraw-Hill, 1957.
- [17] *VDI-Wärmeatlas*, VDI Verlag, ISBN 3-18-400760-X, 1988.
- [18] *Dubbel - Taschenbuch für den Maschinenbau*, Springer, ISBN 3-540-18009-5, 1987.
- [19] *Handbook of Technical & Engineering Ceramics - Part 1 : An Introduction for the Engineer and Designer*, Her Majesty's Stationary Office, ISBN 0-11-480052-9, 1985.
- [20] *Aide-mémoire de résistance des matériaux*, Mir, 1979.
- [21] *Système de fixation pour les tuiles de la colonne centrale et des angles intérieurs de la chambre à vide de TCV*, INT 192/97, 1997.
- [22] *Methode der finiten Elemente*, Zienkiewicz, Carl Hanser Verlag, ISBN 3-446-12525-6, 1984.

